Annu. Rev. Biomed. Eng. 2000. 02:511–50

WAVELETS IN TEMPORAL AND SPATIAL PROCESSING OF BIOMEDICAL IMAGES

Andrew F. Laine
Department of Biomedical Engineering, Columbia University, New York, New York 10027; e-mail: laine@columbia.edu

Key Words wavelet, multiscale, time-frequency, image processing, imaging

■ **Abstract** We review some of the most recent advances in the area of wavelet applications in medical imaging. We first review key concepts in the processing of medical images with wavelet transforms and multiscale analysis, including time-frequency tiling, overcomplete representations, higher dimensional bases, symmetry, boundary effects, translational invariance, orientation selectivity, and best-basis selection. We next describe some applications in magnetic resonance imaging, including activation detection and denoising of functional magnetic resonance imaging and encoding schemes. We then present an overview in the area of ultrasound, including computational anatomy with three-dimensional cardiac ultrasound. Next, wavelets in tomography are reviewed, including their relationship to the radon transform and applications in position emission tomography imaging. Finally, wavelet applications in digital mammography are reviewed, including computer-assisted diagnostic systems that support the detection and classification of small masses and methods of contrast enhancement.

CONTENTS

1523-9829/00/0825-0511$14.00

INTRODUCTION

In this section, we describe the motivation for wavelet and other linear time-frequency localization transforms, explain how the simplest wavelet transforms are computed, and point to some of their mathematical properties. We then discuss several of the many generalizations that have been developed and are needed for specific applications.

There now exists considerable literature on wavelets and related time-frequency transforms, which is aimed at many different audiences. Among the textbooks on signal processoring, those by Vetterli & Kovacevic (1), Strang & Nguyen (2), and Mallat (3) cover a wide range of different approaches. Vetterli & Kovacevic are linked most closely to DSP; Strang & Nguyen aim to lay a bridge between DSP and mathematical analysis; and Mallat is the most wide-ranging of the three. A slightly older text, also covering several angles, is that of Daubechies (4). Details about the materials summarized in the initial section of this review can be found in all of these books, as well as in virtually every textbook on wavelets, together with many primary reference citations (4a). We have therefore left out detailed references in these first subsections; later in this review, we provide detailed references to material that is not as widely available in textbooks. Other reviews of wavelets in biomedical applications can be found, for example, in works by Unser & Aldroubi (5) and by Unser (6).

Motivation

Wavelets constitute a tool to decompose, analyze, and synthesize functions, with an emphasis on time-frequency localization. A simple wavelet decomposition of a function f of time t can be written as the expansion

$$f(t) = \sum_{j,k\in\mathbb{Z}} c_{j,k}\psi_{j,k}(t) \tag{1}$$

For the moment, the variable t is one-dimensional (1-D), but we can also deal with higher dimensions (see below). In the above equation, the functions $\psi_{j,k}$ are the wavelets; they are generated by scaled and translated versions of a "parent" function ψ, in the following way:

$$\psi_{j,k}(t) = 2^{j/2}\psi(2^j t - k) \quad \text{for } j, k \in \mathbb{Z} \tag{2}$$

We have restricted our attention mainly to square integrable wavelets ψ with certain properties. The basic requirements are that ψ be well localized in both time and frequency and that ψ be an oscillating function; mathematically, this last requirement is made explicit by requiring that $\psi \in L^1$ and $\int \psi = 0$. In practice, we often make the more stringent requirement that the Fourier transform $\hat{\psi}$ of ψ be mostly concentrated on a region away from zero; that is, ψ should be a bandpass function; with the normalizations implicit in Equation 1, this concentration region would consist of (essentially) the union of two intervals, $[-2\pi, -\pi] \cup [\pi, 2\pi]$.

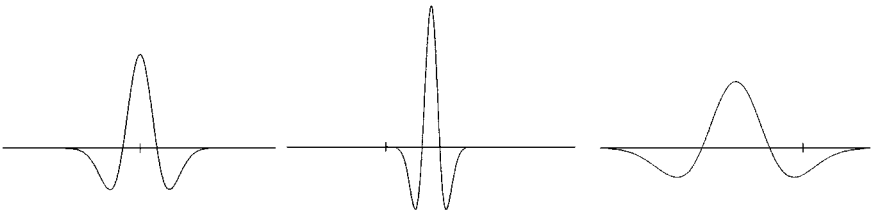

Figure 1 The "Mexican hat" wavelet $\psi(x) = (1 - x^2)e^{-x^2/2}$ (*left*), together with two examples of translates and dilates. (In each case, the tick corresponds to $x = 0$.) For this ψ, the $\{\psi_{j,k}\}$ values do not constitute an orthonormal basis.

Figure 1 shows diagrams of a possible generating wavelet ψ and two scaled and translated versions of it. The dilation (indexed by j) affects the wavelet by shrinking or stretching its support; normalizing, as in Equation 2, which ensures that all of the $\psi_{j,k}$ wavelets have the same energy, also affects their amplitude. Note that the dilation can also be interpreted as changing the frequency concentration of the wavelets; whereas ψ is mostly localized in frequency in the band $[\pi, 2\pi]$, $\psi_{j,k}$ is localized in frequency mostly in $[2^j\pi, 2^{j+1}\pi]$. The parameter k indicates where in time the wavelets are localized; because $\psi(2^j t - k) = \psi[2^j(t - 2^{-j}k)]$, the wavelet $\psi_{j,k}$ is localized near $t = 2^{-j}k$, and because k moves with unit steps, we use a translation step 2^{-j} at scale j. Wavelet families exist for which one does not dilate systematically by multiples of 2 and many other generalizations; for this introduction, we assume multiples of 2.

The $\psi_{j,k}$ wavelets are thus localized in frequency and in time; the expansion (Equation 1) therefore corresponds to a time-frequency localized expansion. There are many frameworks in physics, engineering, computer science, and mathematics, in which time-frequency expansions are useful, and ideas from all of these different fields have contributed to the development of wavelets and related tools.

A well-known and much older time-frequency–localized expansion is given by the windowed Fourier transform, in which functions f to be analyzed are similarly written as a superposition of elementary building blocks, now obtained by modulating and translating an envelope function:

$$f(t) = \sum_{m,n\in\mathbb{Z}} a_{m,n} g^{m,n}(t) \tag{3}$$

where $g^{m,n}(t) = e^{-im\omega_0 t} g(t - nt_0)$. If the window function g is well localized in time and frequency, for instance, $\sim t = 0$, and around zero frequency (there is no need to require that g be essentially bandpass in this case; approximately bandlimited g values suffice), then each $g^{m,n}$ is localized at around $m\omega_0$ in frequency and around nt_0 in time.

Time-frequency–localized expansions and their generalizations to higher dimensions (for images, one should then talk rather about an expansion with localization in space as well as in spatial frequency) are used in many different contexts.

They help break complicated signals into simpler components and may therefore be useful in the analysis or segmentation of such complex signals, in the recognition or detection of particular features, and in compression as well as denoising. Below, various applications illustrating these uses are presented.

The difference between a wavelet transform and a windowed Fourier transform lies in how each achieves time-frequency localization. By their construction, high-frequency wavelets are very narrow; they pack all of the oscillations of the basic wavelet into a small interval; low-frequency wavelets, obtained by stretching the basic wavelet, are much wider (see Figure 1). In contrast with a wavelet transform, the basic building blocks in a windowed Fourier expansion are all given by translating a given window and using it as an envelope for a range of frequencies, as shown by the definition of the $g^{m,n}$ above; these functions have therefore all of the same "width" in time as g itself. (This fact is also illustrated by Figure 7*a* and *b* below.) Which of the two transforms is the most useful depends on the types of signals analyzed. If the signal consists mostly of time-harmonic components, which, even at high frequencies, have a long correlation time, then a windowed Fourier transform, with building blocks that share these characteristics, is best. If the signal consists of a wide range of frequencies, with much shorter correlation times for the high frequencies than for the low frequencies (which is typically the case with transients superposed on more slowly changing components or short-lived transients between smoother parts of the signal), then the "zoom-in" quality of the wavelet transform is more useful, because it has a very small field of vision for high frequencies but can be used to view low frequencies at a larger scale. Figure 2*a* and *b* are caricatures of signals that are natural candidates for efficient representation via a windowed Fourier analysis vs a wavelet analysis.

As discussed below, some applications work best with tools that can be viewed as intermediate between wavelets and windowed Fourier transforms.

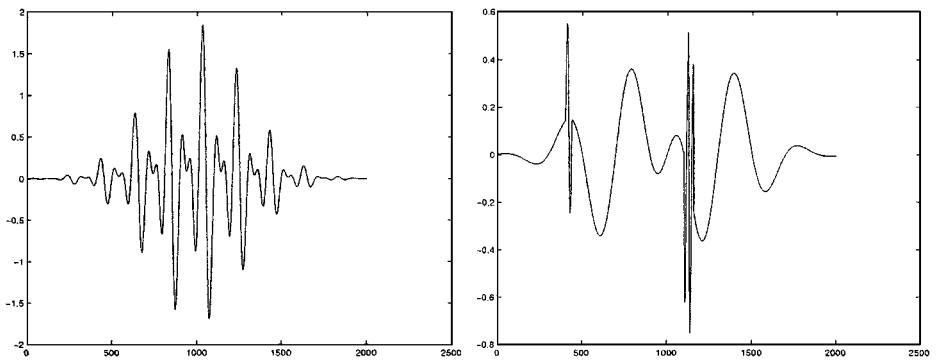

Figure 2 (*a*) A simple example of a signal for which a windowed Fourier transform is better suited than a wavelet transform. (*b*) A simple example of a signal with transients for which a wavelet transform is better suited than a windowed Fourier transform.

Algorithms

So far we have not addressed how the coefficients in any of the proposed expansions above can be computed. In many applications, the wavelet ψ in a wavelet expansion of type 1 is chosen so that the $\psi_{j,k}$ values constitute an orthonormal family. In that case, the $c_{j,k}$ values are simply given by scalar products with the $\psi_{j,k}$ wavelet values themselves:

$$c_{j,k} = \int f(t)\psi_{j,k}(t)\,dt = \langle f, \psi_{j,k}\rangle$$

This calculation gives an explicit formula, but does not yet solve the problem; if we had to carry out the corresponding large number of integrations to find those coefficients, then the transform would not be practical. Fortunately, smooth and well-localized wavelet bases are also associated with fast transforms. These fast trasforms are linked to the existence, for any reasonable wavelet basis, of an underlying multiresolution analysis. That is, if we denote by $P_J(f)$ a partial sum of Equation 1,

$$P_J(f) = \sum_{j<J}\sum_{k\in\mathbb{Z}}\langle f, \psi_{j,k}\rangle\psi_{j,k}$$

then these partial sums can be viewed as successively finer approximations of f (as J increases). These values of $P_J(f)$ can also be written as

$$P_J(f) = \sum_{k\in\mathbb{Z}}\langle f, \phi_{J,k}\rangle\phi_{J,k}$$

where ϕ, the scaling function, is linked to ψ; for $k \in \mathbb{Z}$, the values of $\phi_{J,k}$, defined in the same way as the $\psi_{j,k}$ in Equation 3, constitute an orthonormal set of functions. Clearly,

$$P_{J+1}(f) = P_J(f) + \sum_{k\in\mathbb{Z}}\langle f, \psi_{J,k}\rangle\psi_{J,k} \tag{4}$$

where the two pieces in the right-hand side are orthogonal. It follows that one can obtain each of these two pieces by performing an appropriate orthogonal projection operation on $P_{J+1}(f)$. More specifically, there exist sequences $(h_n)_{n\in\mathbb{Z}}$ and $(g_n)_{n\in\mathbb{Z}}$ (independent of j) such that

$$\begin{aligned}\langle f, \psi_{j,k}\rangle &= \sum_n g_{n-2k}\langle f, \phi_{j+1,n}\rangle;\\ \langle f, \phi_{j,k}\rangle &= \sum_n h_{n-2k}\langle f, \phi_{j+1,n}\rangle\end{aligned} \tag{5}$$

Carrying out a full fast wavelet transform of this type consists then in the following two steps.

1. Starting from fine-scale samples of f, of the type $f_k = f(2^{-J}k)$, the scalar products $s_{J,k} = \langle f, \phi_{J,k}\rangle$ are computed, which can be done by a simple preprocessing filter; because $s_{J,k} = 2^{-J/2}[f(2^{-J}k) + O(2^{-J})]$, it often

suffices, for signal analysis applications, to use the approximation $s_{J,k} \approx 2^{-J/2} f(2^{-J}k)$.

2. Next, as many levels as desired are computed by filtering and down-sampling, corresponding to Equation 5:

$$s_{j,k} = \sum_n h_{n-2k} s_{j+1,n}; \quad c_{j,k} = \sum_n g_{n-2k} s_{j+1,n} \tag{6}$$

The values of $c_{j,k}$ are then the desired wavelet coefficients, that is, coefficients such that Equation 1 holds. In practice, one often stops at some coarsest level (which we set to be $j = 0$, for convenience), effectively replacing Equation 1 by

$$f(t) = \sum_{k\in\mathbb{Z}} s_{0,k}\phi_{0,k}(t) + \sum_{j=0}^{J-1} \sum_{k\in\mathbb{Z}} c_{j,k}\psi_{j,k}(t) \tag{7}$$

noting that we have no coefficients beyond the finest-scale J here, because no finer-scale information on f can be derived from only the samples $f(2^{-J}k)$. Because the transform $(s_{J,k})_{k\in\mathbb{Z}} \rightarrow [(c_{j,k})_{0\le j<J,k\in\mathbb{Z}}, (s_{0,k})_{k\in\mathbb{Z}}]$ is orthonormal, it can be inverted by the transpose operation; more specifically, for all j,

$$s_{j+1,n} = \sum_k [h_{n-2l} s_{j,l} + g_{n-2l} c_{j,l}] \tag{8}$$

Together, decomposition and reconstruction Equations 6 and 8, respectively, can be represented in block diagram format, which is familiar to electrical engineers, as shown in Figure 3.

The fast-wavelet transform is therefore simply a critically sampled subband filter bank with exact reconstruction.

In Figure 4, we show the plot of a wavelet $\psi(t)$ and of the absolute value of its Fourier transform, for an orthonormal wavelet family, corresponding to FIR filters H and G of length 20.

Mathematical Properties

Wavelet transforms have many mathematical properties that stem from their ability to "zoom in" on singularities. For instance, we can characterize the smoothness of

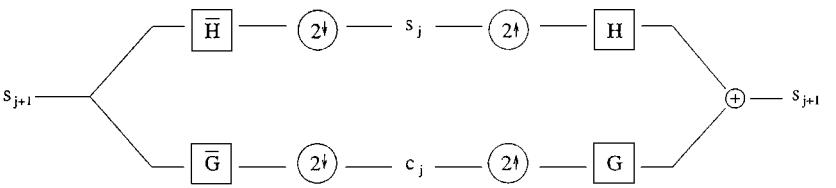

Figure 3 Block diagram corresponding to Equations 6 and 8 (see text).

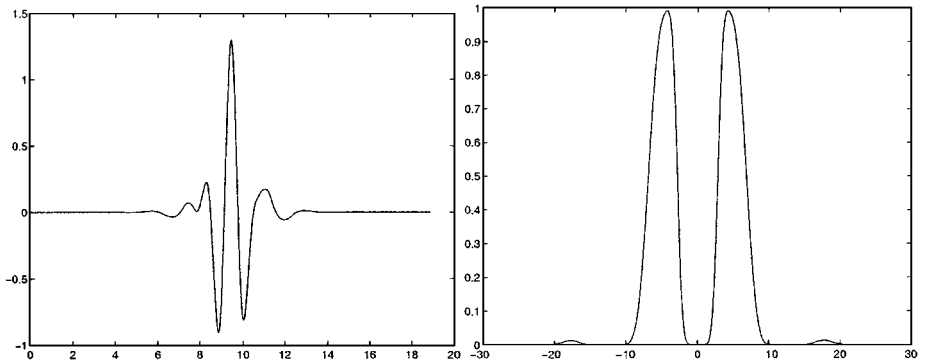

(*a*) (*b*)

Figure 4 (*a*) An example of a wavelet ψ for which the $\psi_{j,k}$ values constitute an orthonormal basis. This ψ is identically zero outside an interval of length 19; it corresponds to a fast wavelet transform with FIR filters with 20 taps. (*b*) Absolute value $|\hat{\psi}|$ of the Fourier transform of the function in panel *a*.

a function by the rate of exponential decay in j of its wavelet coefficients $c_{j,k}$:

$$\int \left| \frac{d^l}{dt^l} f(t) \right|^2 dt < \infty \Leftrightarrow \sum_{j,k \in \mathbb{Z}} 2^{2jl} |c_{j,k}|^2 < \infty$$

This can also be used locally, that is, around individual times t. In this case some extra mathematical conditions of a technical nature are needed to make rigorously correct statements (see references below); "morally," it is still the case that the smoothness of f at t_0 is given by the rate of decay in f of $\max\{|c_{j,k}|; k \in S_j(t_0)\}$, where $S_j(t_0)$ is the set of indices k for which t_0 is in the support of $\psi_{j,k}$ (typically, this means that $|t_0 - 2^{-j}k| \leq 2^{-j}L$, where L is the length of the FIR filters H and G).

Concretely, this means that we can classify different times t (or, for images, different positions in the image) by how fast the associated wavelet coefficients decay; this classification method enables one to find edges or other special features. Adjusting, at those special locations, the decay rate of these $c_{j,k}$ values can then be used to enhance those features. This step is used, for instance, in the mammography applications below. Characterization of smoothness of a function by the decay of its wavelet coefficients is but one example of a mathematical property of wavelets that can be very useful in applications. More mathematical properties, with applications in signal analysis, are discussed by Mallat (3) and Meyer (7).

Higher Dimensional Wavelet Bases

In one dimension, the Fourier transform $\hat{\psi}$ is mostly concentrated on $[-2\pi, -\pi] \cup [\pi, 2\pi]$, if the values of $\psi_{j,k}$ defined by Equation 3 constitute an orthonormal basis (see Figure 4*b*). The Fourier transform $\hat{\psi}$ of the accompanying scaling function

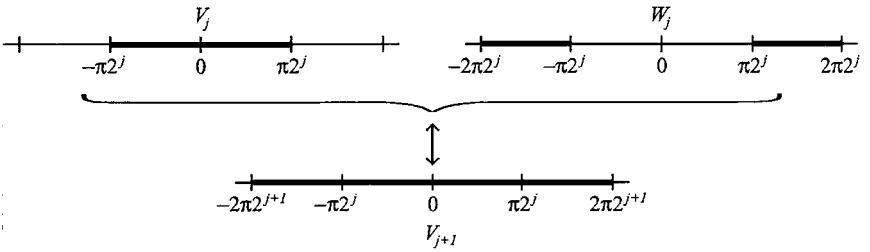

Figure 5 Projection of f onto V_j or W_j "captures" the frequency content of f for $|\xi| \leq \pi 2^j$ or $\pi 2^j \leq |\xi| \leq 2\pi 2^j$, respectively; together, this information is equivalent to capturing the frequency content of f for $|\xi| \leq 2\pi 2^j$, that is, the projection of f onto V_{j+1}.

ψ is concentrated on $[-\pi, \pi]$. More generally, the values of $\psi_{j,k}$, for fixed j, span a space of functions W_j with Fourier transforms concentrated on $\pi 2^j \leq |\xi| \leq 2\pi 2^j$; the values of $\phi_{j,k}$ span V_j, consisting of functions with Fourier transforms concentrated on $|\xi| \leq \pi 2^j$. Equation 5, corresponding to the transition from $V_{j+1} = V_j \oplus W_j$ to the two component spaces V_j and W_j, and its converse (Equation 6) can schematically be represented as in Figure 5. (Note that this is a schematic representation only; the filters in an orthonormal wavelet transform are not sharp cut-off filters in frequency. Because all of the transforms are orthonormal, all of the aliasing and distortions that might be a consequence of using nonideal filters are cancelled in the reconstruction of Equations 5 and 6, justifying the schematic representation in Figure 5.)

With this interpretation of the 1-D wavelet transform, it is now easy to define a two-dimensional (2-D) wavelet transform that has similar features. Figure 6 shows a schematic representation of how the space V_{j+1}, corresponding to ξ with $\max(|\xi_1|, |\xi_2|) \leq \pi 2^{j+1}$, can be split into V_j (corresponding to the central square, i.e. ξ with $\max(|\xi_1|, |\xi_2|) \leq \pi 2^j$) and three additional pieces:

(*a*) $|\xi_1| \leq \pi 2^j, \pi 2^j \leq |\xi_2| \leq 2\pi 2^j$;

(*b*) $|\xi_2| \leq \pi 2^j, \pi 2^j \leq |\xi_1| \leq 2\pi 2^j$;

(*c*) $\pi 2^j \leq |\xi_1| \leq 2\pi 2^j, \pi 2^j \leq |\xi_2| \leq 2\pi 2^j$

The space V_j is spanned by the orthonormal family $\varphi_{j;k_1,k_2}(x_1, x_2) = \phi_{j,k_1}(x_1)\phi_{j,k_2}(x_2)$, where $k_1, k_2 \in \mathbb{Z}$; the three other pieces that, together with V_j, make up V_{j+1}, are spanned by, respectively, $\psi^a_{j;k_1,k_2}(x_1, x_2) = \phi_{j,k_1}(x_1)\psi_{j,k_2}(x_2)$, $\psi^b_{j;k_1,k_2}(x_1, x_2) = \psi_{j,k_1}(x_1)\phi_{j,k_2}(x_2)$, and $\psi^c_{j;k_1k_2}(x_1, x_2) = \psi_{j,k_1}(x_1)\psi_{j,k_2}(x_2)$. The corresponding fast transforms are given, as suggested by these formulas, by implementing Equations 5 and 6 on both rows and columns of a given fine-scale array $(s_{j+1;n_1,n_2})_{n_1,n_2\in\mathbb{Z}}$, leading to two-dimensional arrays s_j (use filter H on both rows and columns), c^a_j (H on row index and G on column index), c^b_j (G on row index and H on column index), and c^c_j (G on both row and column indices).

The same construction can be used in higher dimensions. In d dimensions, this construction uses $2d - 1$ different d–dimensional wavelets, which are usually indexed by the vertices of the cube $[0, 1]^d$ that differ from $(0, \ldots 0)$.

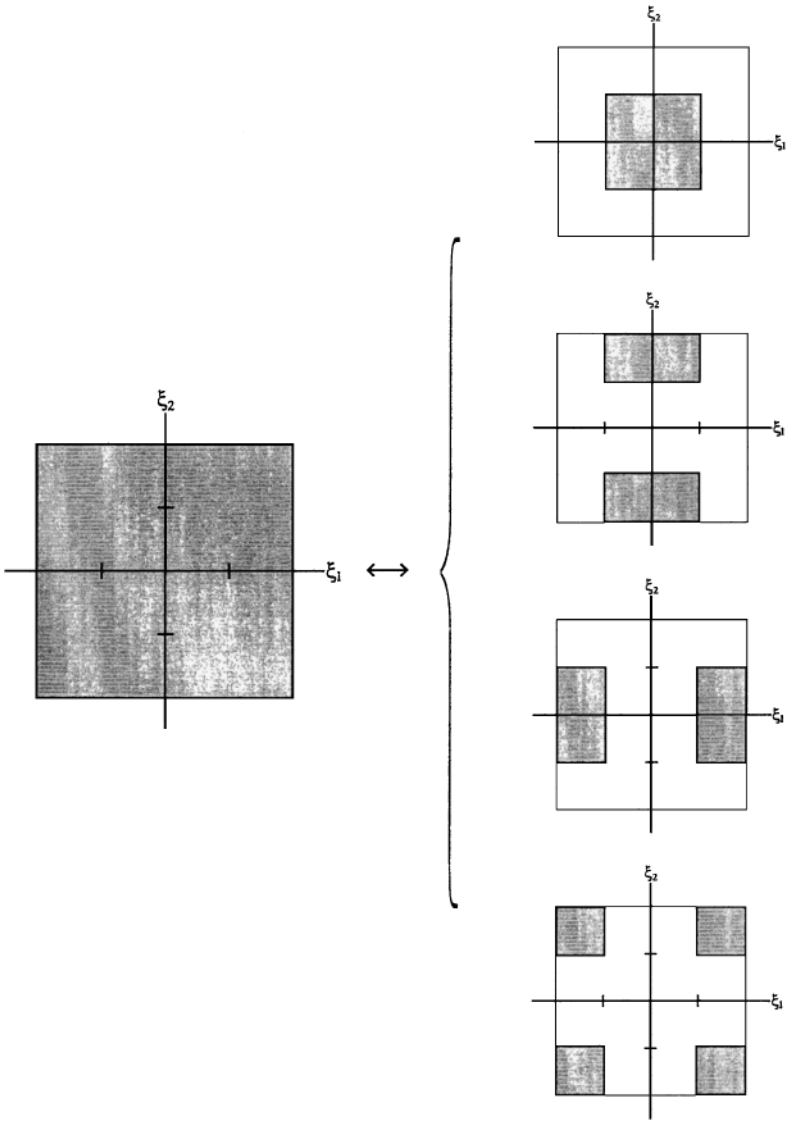

Figure 6 Schematic representation of the decomposition of V_{j+1} into V_j and three additional pieces, for a 2-D–wavelet basis.

There exist many other constructions for multidimensional wavelets, in which the wavelets are not separable (i.e. cannot be written as a product of two 1-D functions); even the dilation underlying the construction can be replaced by a matrix instead of the simple multiplication by 2 that is underlying the formulas above. For practical implementation, the construction given here is often preferable, because it is easier; for certain specific applications, some of the other constructions may offer real advantages, however, making it worthwhile to go to a more burdensome implementation.

One can also construct a 2-D basis, starting from the 1-D orthonormal basis $[\psi_{j,k}(x);\ j, k \in \mathbb{Z}]$ by constructing all of the products $\psi_{j_1,k_1}(x_1)\psi_{j,k_2}(x_2)$ with $j_1, j_2, k_1, k_2 \in \mathbb{Z}$. These constitute an orthonormal basis, but the scaling in the two variables is now decoupled. If the signal under study shows such decoupling in its fine-scale features, then this tensor product basis may be better adapted than the 2-D wavelet basis given above; for images, however, one typically finds that coupling the scaling in the two variables, resulting in a single scale parameter j as above, gives better results.

Generalizations

The wavelet bases discussed above, of which one example is given in Figure 4, are orthonormal bases associated with fast transforms that can be useful for many applications. They are, however, not ideal for all situations. Figure 2*a* illustrates a function for which the windowed Fourier transform is a better tool than the wavelet transform. Even for functions with sharp, well-localized transients, it may be useful to step outside the framework of orthonormal wavelet bases as defined above.

Symmetry A first observation is that the wavelet ψ given in Figure 4*a* is not symmetric; this lack of symmetry is characteristic for all reasonably smooth ψ for which the $\psi_{j,k}$ values defined by Equation 2 generate an orthonormal-wavelet basis corresponding to FIR filters H and G. For certain applications, symmetry is desirable; this can be achieved by switching to generalizations of the orthonormal-wavelet bases illustrated above. One possible generalization is to relinquish orthonormality in a carefully controlled way, so that the resulting wavelets still share many of the important mathematical properties of orthonormal-wavelet bases; in this construction of biorthogonal wavelets (8; see also the textbook references given above), the block diagram of Figure 3 is replaced by a similar diagram, in which the reconstruction filters $\tilde{H}$ and $\tilde{G}$ differ from the decomposition filters H and G. Another possible generalization that retains orthonormality is to introduce, even in one dimension, several wavelets $\psi^1, \ldots \psi^l$, as described by Alpert & Rokhlin (9), Geronimo et al (10), and Strang & Strela (11).

Boundary Effects In practical applications, one never works with an infinite array of data; this means that the constructions above, suited for work on $\mathbb{R}^d$ (or, in

sampled form, on $\mathbb{Z}^d$), must be adapted to finite domains, which can be achieved in several ways. For simple situations, periodizing the problem may suffice; often it is useful to be a little more careful and to introduce specially adapted filters near the boundaries to take care of boundary effects. A construction of such filters is given by Cohen et al (12) for the orthonormal case; a very simple and natural way to construct boundary filters for biorthogonal wavelets is given by Sweldens' lifting scheme [Sweldens (13), Sweldens & Schröder (14); see also Vetterli & Kovacevic (1)].

Translational Invariance Wavelet bases, as defined by Equation 2 or by any of the generalizations mentioned above, are highly noninvariant under translations, as shown by their definition; for scale j, the translation step is 2^{-j}; this scale dependence means that the whole family of building blocks $(\psi_{0,k}; k \in \mathbb{Z}) \cup (\psi_{j,k}; 0 \le j \le J-1, k \in \mathbb{Z})$, used, for example, in reference 7, is invariant only under translations by much large unit steps, which means that the wavelet transform obtained from a shifted version of a data set may differ markedly from the wavelet transform of the original data set. Algorithmically, this result is a consequence of the down-sampling by 2 in Equation 5 or in Figure 3. If the values of $s_{j+1,n}$ are replaced by $\tilde{s}_{j+1,n} = s_{j+1,n+1}$, then the sequences $\tilde{s}_j$ and $\tilde{c}_j$, obtained from filtering and down-sampling $\tilde{s}_{j+1}$, are different from s_j and c_j; in the down-sampling that computes the s_j and c_j, we "throw away" the odd-indexed entries of $\bar{H} \times s_{j+1}$ and $\bar{G} \times s_{j+1}$; the $\tilde{s}_{j,k}$ and $\tilde{c}_{j,k}$ are equal to these missing entries. A simple solution to reintroduce translation invariance is to omit down-sampling at every step. This results in an expansion in a redundant family, by using, at every scale j, where $0 \le j \le J-1$, all of the functions $\psi(2^j t - 2^{j-J} l)$, where $l \in \mathbb{Z}$ (instead of only those for which $l = 2^{J-j}k$ and $k \in \mathbb{Z}$, corresponding to Equation 2); because of the redundancy, these wavelets then have to be renormalized appropriately. The redundant family can also be viewed as the union of several different orthonormal bases, with the special property that computing all of the coefficients in the 2^J different bases can be done in $O(N \log N)$ operations, starting with N data of type $f(2^{-J}k)$, where $n_0 \le k \le N + n_0$. (In a variation on this idea, one can also choose to forgo down-sampling at only the first J_0 levels, resulting in 2^{J_0} different bases, and translation invariance for steps of width 2^{-J_0} instead of the smaller-width 2^{-J}.) Such redundant representations have been shown to be very useful in noise reduction (15) or in detection and parameter extraction. Some applications described below use this type of translation-invariant, redundant wavelet transform.

Orientation Selectivity As shown in Figure 5, the standard definition of higher dimensional wavelets leads to bad orientational localization. This is particularly apparent for ψ^c, which localizes around the direction $\xi_1 = \xi_2$ as well as around the orthogonal direction $\xi_1 = -\xi_2$. Several solutions have been proposed and used to address this. If one uses the same construction to go from one to two dimensions, as explained earlier, starting, however, from complex functions ψ and ϕ that concentrated mostly on one half of the frequency axis (see 4 for an example), then

the resulting 2-D basis will concentrate mostly around only one of the directions, namely $\xi_1 = \xi_2$, at the price of having to work with complex wavelets. (Note that this approach introduces redundancy if one works with real signals only, because N real data are transformed into N complex coefficients or $2N$ real numbers.) Other constructions that similarly introduce a complex transform and that lead to even better separation of different quadrants in the frequency plane are given by brushlets (see 16). We describe some applications below in which brushlets are used, because of their better orientation selectivity, compared with normal wavelet bases. There also exist constructions that have even better orientation selectivity, at the cost of being nonseparable and even more redundant, such as the steerable filter banks of Freeman & Adelson (17), which they applied to biomedical imaging.

Time-Frequency Tiling Figure 7*a* and *b* illustrate the difference in time-frequency localization between the windowed Fourier transform and the wavelet transform. For both types of transform, there exist variants that adapt, to some extent, the time-frequency tiling.

In a standard wavelet transform as described above, one computes at every scale a set of wavelet coefficients ($c_{j,k}$) and scaling coefficients ($s_{j,k}$); the $c_{j,k}$ coefficients are stored as such (or post-processed later, if desired); the $s_{j,k}$ coefficients have to undergo further filtering and down-sampling. This procedure leads to progressively narrower frequency bins as one descends to lower frequencies and correspondingly

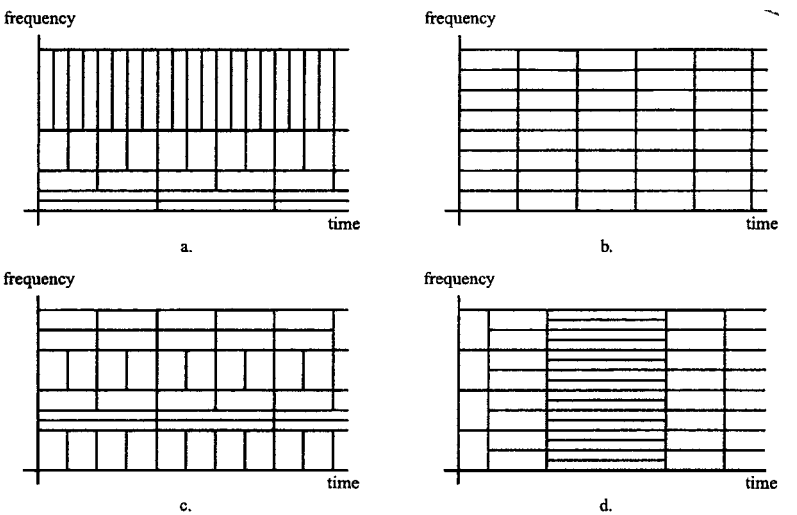

Figure 7 Schematic representation of the time-frequency localization for different bases. Panel: (*a*) Wavelets, (*b*) windowed Fourier transform (or local cosine transform with fixed window), (*c*) a wavelet packet basis, and (*d*) a local cosine transform with various windows. In all cases, this is a schematic representation only. In each case, the basis functions do in fact overlap in time and in frequency.

wider time spreading (see Figure 7*b*). If not only the $s_{j,k}$ but also the $c_{j,k}$ are filtered and down-sampled, then one can introduce similar frequency band splitting at higher frequencies, which means that every time we have performed a convolution (with either $\bar{H}$ or $\bar{G}$) and down-sampling, we have had the choice either to keep the resulting coefficient sequence as is or to replace it with two sequences, obtained by convolving by $\bar{H}$ and $\bar{G}$ and down-sampling. Every combination of choices leads to an expansion in a corresponding orthonormal wavelet packet basis. Figure 7c gives an example of the time-frequency localization corresponding to one such wavelet packet basis choice. [Note that, for each such tiling, one can construct special filter banks, not obtained by cascading the simple filters H and G, that will do an even better job of localizing closely to that tiling. The interesting aspect of wavelet packets is that the cascading structure allows, again with $O(N \log N)$ operations for N data, computation of coefficients for a large number of different bases, making it possible to adapt the basis to the data (see below).]

The windowed Fourier transform described above does not lead to interesting bases with good localization in time and frequency. It is interesting that this obstruction no longer exists if one replaces complex exponentials by cosines or sines, as shown by the constructions of Malvar (18) and Coifman & Meyer (19). It turns out, moreover, that it is then possible to use different overlapping windows with various lengths. Concretely, the basis functions are then

$$g^{m,n}(t) = \sqrt{\frac{2}{l_n}} \cos\left[\pi\left(m + \frac{1}{2}\right)\frac{t - t_n}{l_n}\right] w_n(t)$$

where the window functions w_n are concentrated mostly on $[t_n, t_{n+1}]$ and $l_n = t_{n+1} - t_n$; the w_n functions overlap with their neighbors and have to satisfy certain technical conditions. [For details, see the original references or Wickerhauser (20), Auscher et al (21), or the textbooks quoted earlier.] Figure 7*d* gives the time-frequency localization of an example of such a local cosine basis.

Best-Basis Selection Coifman & Wickerhauser (22) proposed to take advantage of the fast simultaneous transform into many different wavelet packet bases by choosing, after the transform, the basis that gave the most compact representation of the data. The same idea can be used for other fast simultaneous transforms or to regroup windows in a local cosine transform, leading to adaptive window length selection. The searches for the best basis within a family are typically implemented through a tree algorithm.

One can even decide to use several bases, when different components of the signal have such widely different characteristics (e.g. harmonic components vs transients in sounds and edges vs texture in images) that they are most efficiently represented in different bases; this approach is sometimes called basis pursuit, and its approximation properties are mathematically less well understood at present. See Mallat (3) or Wickerhauser (20) for more details.

WAVELETS IN BIOMEDICAL IMAGING: Analysis and Quantification

In this section, we review some of the more recent applications of wavelets in biomedical imaging. We first describe methods of denoising magnetic resonance (MR) imaging (MRI) signals to improve the signal-to-noise ratio (SNR) in functional imaging. In addition, we review previous wavelet-based encoding schemes for MRI and present some recent results with complex wavelets. We then review recent applications of wavelets in ultrasound imaging, including denoising and singularity detection in Doppler ultrasound, tissue characterization in cardiac ultrasound, and methods of boundary detection for quantification of cardiac volumes. We also report on a method of analysis that uses an orientation-sensitive basis and computes cardiac output from echos collected from a true 3-D transducer. Next, we summarize previous work related to wavelets in computed tomography. This area is one of the most rigorously studied applications and includes relationships between the radon transform, limited angle tomography, the wavelet-vaguelette decomposition, and more recent nonlinear approaches that attempt to overcome the limitations of single-valued decomposition methods. Finally, we review applications in the area of digital mammography, including methods of contrast enhancement and detection of masses. We describe some recent efforts to develop computer-aided diagnostic (CAD) systems that incorporate wavelet-based methods of lesion detection. We also describe the need to use nonlinear methods for enhancement of subtle mammographic features in dense radiographs.

Wavelet Applications in Magnetic Resonance Imaging

Applications of the wavelet transform are appearing in conventional MRI, as well as in functional MRI (fMRI). First, we review postprocessing techniques of MRI and fMRI data with wavelets and then discuss wavelet-encoding schemes.

Denoising and Enhancement of Magnetic Resonance Imaging Data Among the first to take advantage of the properties of wavelet analysis for MRI, Healy et al (23, 24) described simple and effective techniques for image denoising and contrast enhancement based on extraction of multiscale edges. Separable cubic spline wavelets, as first derivatives of the corresponding scaling function, were applied to image data to obtain multiscale gradients. The scaling function performed as a smoothing operator that stabilized the gradients against noise. From the multiscale gradients, multiscale edge representations were computed as local maxima of gradient magnitudes along the direction of each gradient. These multiscale edge representations were then processed for noise removal or contrast enhancement. After that, image reconstruction was performed in two phases: (*a*) reconstruction of multiscale gradients from edge representation through alternate projection onto a set of wavelet-reproducing kernels and onto a set of consistency constraints and (*b*) image reconstruction through an inverse wavelet transform.

The general concept of multiscale edge representation and the corresponding image reconstruction process were previously developed by Mallat & Zhong (25, 26). However, in Healy's paper, processing for noise removal included the construction of tree structures of multiscale edges (tracing of edges through scale space) and thresholding of the tree branches via a metric computed for each branch (a product of gradient magnitude and "length" of branch). The underlying assumption of this algorithm was that key features of the image (signal) would persist through scale space, that is, exist at multiple scales, whereas edges caused by noise would appear only at finer scales and would be lower in magnitude. For contrast enhancement, the magnitude of multiscale edges was stretched, either by a constant factor k for all scales or by a set of scale variable factors k_j (different ks for each scale). The latter approach attempts to suppress noise amplification at small scales. A combination of denoising and enhancement has also been applied. Promising results were observed, although a tradeoff between noise removal and preservation of image details was also observed. Further optimization for threshold selection and edge stretching remains to be achieved.

Another interesting algorithm with the wavelet transform for denoising MRI data was presented by Nowak (27). His work was based on the assumption that MR images should be modeled by the Rician distribution (28, 29). Rician noise is non-zero mean and depends on local signal intensity. It introduces a signal-dependent bias to the observations, which can reduce the contrast of an image. For a high SNR, Rician noise tends to the Gaussian distribution. Because of this complication, estimation from noisy data is especially challenging in MRI. Nowak proposed two wavelet domain-filtering algorithms to estimate a signal s from its magnitude image x. Wavelet coefficients d_I of an image were computed and modified for $\hat{d}_I = \alpha_I \cdot d_I$, where the collections of α_I resembled a wavelet domain filter. One algorithm derived α_I under an assumption of Gaussian noise and worked well for high SNR. Another algorithm operated on the squared-magnitude MR image. Using the properties of the wavelet transform and the noncentral chi-square distribution, Nowak showed that wavelet coefficients of the squared-magnitude values of x^2 are unbiased estimators of wavelet coefficients of the squared signal s^2. Furthermore, the scaling coefficients of the squared-magnitude image were biased estimators by a constant value. Building on these observations, the second algorithm removed the bias as well as noisy wavelet coefficients, providing improved image contrast for high SNR and low SNR. Results have been shown for simulated data, MRI data, and low SNR MRI data (27).

fMRI is an important emerging technique in the field. Here wavelets have been mainly used for noise removal and detection of activation areas in the brain. Next we describe these applications after a brief overview of fMRI principles.

Functional Magnetic Resonance Imaging fMRI is a noninvasive method of measuring spatially distributed brain activity as a function of local vasodilations (30). A local vasodilation is characterized by the hemodynamic response, which is slow and has a time scale on the order of seconds. fMRI techniques are

based on the changes associated with the ratio of oxyhemoglobin to deoxyhemoglobin, commonly referred to as the "BOLD" (blood oxygenation level dependent) effect. Oxyhemoglobin is diamagnetic, whereas deoxyhemoglobin is paramagnetic. As the erythrocytes are confined to vasculature, the change in the ratio of oxy/deoxyhemoglobin causes magnetic susceptibility variations locally. Protons diffusing through this region have dephasing effects. Thus, an MR sequence that is sensitive to a magnetic susceptibility variation can be used in a temporal sequence to observe these changes in signal as a function of time (30, 31). Typically, an echo planner gradient echo sequence is used for image acquisition. Basically, this implies that the level of blood oxygenation acts as an inherent contrast agent, giving rise to temporal signal changes of $T2^*$ that are $\sim$2%–6% from a baseline (resting state) to an activation state.

Owing to the small magnitude of the detectable signal, scanner-induced noise, and intrinsic biological heterogeneity, the images typically have poor SNRs. Problems with BOLD methods have been attributed to the presence of artifacts that are associated with head and/or vessel motion (32), as well as vascular inflow (33, 34) and drainage effects (35). Hence, detection and localization of areas of activation are difficult tasks that challenge the state of the art.

Denoising in Functional Magnetic Resonance Imaging To improve the SNR of fMRI data, wavelet-based denoising schemes have been applied before detection of activation. Hilton et al (36) computed an orthonormal wavelet decomposition and applied a nonlinear soft-thresholding operation to each coefficient at the finer scales. The denoising operator was formulated as (37, 38):

$$T_S(f,\lambda) = \begin{cases} f-\lambda & \text{if } f \geq \lambda \\ f+\lambda & \text{if } f \leq -\lambda \\ 0 & \text{if } |f| \leq \lambda \end{cases} \tag{9}$$

Of fundamental importance to signal recovery is the choice of the threshold λ. Global and data-driven approaches have been investigated. The first method was the "VisuShrink" universal threshold introduced by Donoho & Johnstone (37):

$$\lambda = \sigma\sqrt{2\log(n)}$$

where n is the number of data samples. Because typically the true value of the standard deviation σ of the noise is not known, it is estimated by $\tilde{\sigma} = MAD/0.6745$, where *MAD* is the median absolute value of the finest-scale wavelet coefficients (37). The second method used was a data-analytic approach that considered both the magnitudes and spatial relationships of empirical wavelet coefficients when determining λ. A threshold $\lambda\nu$ was selected separately for each level ν of coefficients by examining the coefficients at each level and recursively removing large coefficients, until the remaining coefficients resembled a sequence of white noise, based on some given criterion. This approach assumed data of a Gaussian distribution. An orthogonal wavelet transform of this data then yielded empirical coefficients that

had independent normal distributions with variance σ^2 and means $\mu_1, \ldots, \mu_n$. Statistical testing of the null hypothesis H_0, that coefficients only contain noise $\mu_n = 0$, then was used to determine coefficients containing mostly signal. These selected coefficients were removed and tests repeated, until the remaining set of coefficients behaved as white noise. Finally, the threshold $\lambda\nu$ was set to σ times the largest coefficient (in absolute value) in each set, the amount by which all of coefficients in the corresponding level were shrunk. After denoising, detection of activation was performed on fMRI data sets by a standard *t*-test. The effect of denoising on the analysis was measured by an increase or decrease in the magnitude of the *t*-statistic, because an increase of the *t*-statistic corresponds to the improved discriminating power of the test. Although reported results were mixed for different data sets (increase, nearly no change, and decrease), Hilton et al suggest a potential for thresholding strategies by using wavelet representations (36).

Activation Detection in Functional Magnetic Resonance Imaging Ruttimann et al (39) proposed a wavelet-based procedure for fMRI analysis to detect activated regions of the brain that correspond to a simple activation task (finger tapping). Their method benefited from the fact that a smooth and spatially localized signal can be represented by a small set of localized wavelet coefficients, whereas the power of noise is uniformly spread throughout a wavelet transform space. By applying an orthogonal wavelet decomposition to averaged difference images of "on" and "off" blocks, a two-step statistical-testing procedure was developed. First, wavelet-space partitions with a large SNR were located, followed by subsequent testing for significant wavelet coefficients that were restricted within these partitions. This resulted in a higher SNR and a smaller number of statistical tests, yielding a lower detection threshold compared with purely spatial-domain testing and, thus, a higher detection sensitivity without increasing type I errors (i.e. reject H_0 when, in fact, H_0 is true). Here the authors assume that the difference images and $g_i(\vec{n})$ ($\vec{n}$ is the pixel location) can be characterized by $g_i(\vec{n}) = f(\vec{n}) + e_i(\vec{n})$, where $f(\vec{n})$ is an unknown deterministic signal that is common to all replications and $e_i(\vec{n})$ is a homogeneous random field of identically and independently distributed Gaussian noise, $iid \sim N(0, \sigma^2)$. The distributions for the individual wavelet coefficients for each of the *m* directional channels at resolution level *j* are then derived. After selecting channels of significant signal power, the estimated signal $\tilde{f}$ was reconstructed through an inverse wavelet transform from the significant coefficients of these channels, selected from a two-sided *z*-test with an overall significance level. The procedure was applied to two different imaging protocols for fMRI, PRESTO, and echo planar imaging (EPI), and results were compared with those from testing in the spatial domain. In general, the activation areas detected with the wavelet method were at similar locations, but were more compact and smoother compared with pure spatial-domain testing. This observation was more pronounced for the PRESTO protocol than for EPI, owing to inherent signal properties of image acquisition (lower SNR of PRESTO). In addition, a crude estimation of the signal bandwidth could be obtained from the first testing stage

as 2^{-j*} times the sampling rate, with j^* the smallest j (highest-resolution level), where at least one of the directional channels carried significant signal power.

In another approach, wavelet and statistical analyses were jointly applied to achieve activation detection (40). In addition, multidimensional wavelet analysis has been used (41). Moreover, denoising of fMRI data through monotonic filtering, similar to wavelet-based methods, has been proposed (42).

Other applications of the wavelet transform to MRI data include truncation artifact reduction by Kok et al (43). Truncation artifacts in MR images stem from the truncation of complex MR data in the Fourier domain (k-space). It was shown that the application of a wavelet shrinkage algorithm (37, 38) to MR images reduced these artifacts. A soft-thresholding procedure was used in this case. Optimal performance of truncation artifact reduction by wavelet-based thresholding, compared with other bases, was shown with a strong definition of artifact-free truncation. Shift-invariant transforms outperformed decimated ones (43). More recently, a wavelet compression method was used to reduce model information for active appearance models (44), which also included training sets of MR images. Further work has been done in denoising of diffusion maps from MR acquisition (45), MR image compression (46, 47), and segmentation of blood vessles in MR flow-sensitive imaging (48).

Finally, in a related paper, denoising of electron microscopic images with wavelets was described (49).

Wavelet-Encoding Schemes for Magnetic Resonance Imaging The use of a wavelet transform to encode has been described in various 2-D and 3-D MRI applications (50–53). In contrast to conventional phase encoding, in which orthonormal Fourier harmonics are used to encode spins across an entire field of view (FOV), wavelet encoding uses an orthogonal set of spatially localized functions. This encoding scheme offers the immediate potential of localized or focused imaging and direct motion artifact reduction. The design flexibility of such encoding may even help to develop a variety of new NMR sequences. However, practical applications of wavelet encoding have been limited so far because of low SNRs and vulnerability to artifacts.

Conventional Fourier phase encoding weights all spins within an entire FOV at each step, with a constant but phase-modulated complex-encoding profile (i.e. a Fourier harmonic). With wavelet encoding, spins are weighted at each step with a spatially localized profile. As a consequence, the inherent SNR is low. In addition, spins are encoded with distinct flip angles. Thus all spins do not experience the same excitation and relaxation sequence. This can complicate image contrast and interfere with wavelet encoding. When sufficient relaxation is absent, such as for a large flip angle or short repetition time (TR), care must be taken to minimize the spatial variance of spin relaxation across an entire FOV. Otherwise, severe artifacts may occur. In case spin relaxation is dominated by a wavelet encoded radio-frequency (rf) pulse such as in a 3-D gradient echo sequence (53), proper encoding order can increase effective TR substantially.

However, wavelet encoding schemes offer great flexibility, because a set of orthonormal encoding profiles can be constructed from any scaling/wavelet function set by proper spatial translation and dilation (4, 54). For a given true encoding resolution and spatial support, a scaling function $\phi(t)$ and wavelet function $\psi(x)$ pair should be designed with the following goals in mind: (*a*) maximum energy $\int \phi^2(x)dx$ and $\int \psi^2(x)dx$, while maintaining the same peak amplitude to maximize the SNR for a given maximum flip angle, (*b*) acceptable rippling (or duration) and peak power of required rf excitation pulses, and (*c*) sufficient reconstruction stability in the presence of noise. Sinc and Haar (50) bases are two extreme cases. Most studies in the literature have adopted Lemarie-Battle and Daubechies bases from existing wavelet processing paradigms (51–53). As an alternative and to best satisfy the conditions above, an array of real as well as complex scaling and wavelet functions was designed and verified through simulations (55). The concept of wavelet encoding has also been extended to other basis functions, as adapted waveform encoding (24). Common to all of these encoding schemes is that phase encoding is replaced by an rf pulse excitation with a wavelet- or more general waveform-shaped excitation profile along the y-axis, $\psi(y)$. The signal produced is then simply the inner product of the excited profile with the spin density along the y-axis. Waveforms that have been reported in the literature include wavelet packets (22), line scans (impulse profiles), Hadamard, and multiple Hadamard functions (24).

Because wavelet encoding relies on selective rf pulses in the presence of a linear gradient to produce orthonormal encoding profiles, it remains to rf hardware imperfections. Modulator side-band suppression leakage and quadrature phase error, transceiver offsets, and nonlinearity are precalibrated and adjusted before data acquisition. To avoid chemical shifts, varying rf waveform and constant gradients are used for wavelet encoding. An rf waveform is first approximated on first order by a Fourier transform of the optimized spatial encoding profiles and then corrected for any nonlinearities between flip angle and NMR signal through numerical iteration so that large flip angles can be used (22, 56). The encoding order can be interleaved to minimize the spatial variance of spin relaxation and also to maximize the effective TR.

An example is given for table-driven wavelet-encoding acquisition and image reconstruction, implemented on a whole-body 4.23 T MRI system at Columbia University (55). Figure 8*a* shows a conventional spin-echo image of a water phantom, constructed with 256 horizontal frequency encodings and 64 vertical gradient phase encodings (TR, 500 ms; TE, 30; NEX, 1; FOV, 200 mm; and slice thickness, 4 mm). Phase encoding was then replaced with a 64-wavelet encoding implemented by the first 90° rf pulse (4-ms duration). Encoding was focused to the central $\frac{1}{4}$ vertical FOV. An optimized spline-based scaling/wavelet function pair at level $M = 3$ was selected to build the orthonormal encoding profiles. The complete set of functions is shown in Figure 9. A sample reconstruction image is shown in Figure 8*b*. It is artifact free and yields superior spatial resolution to that expected from focused encoding alone.

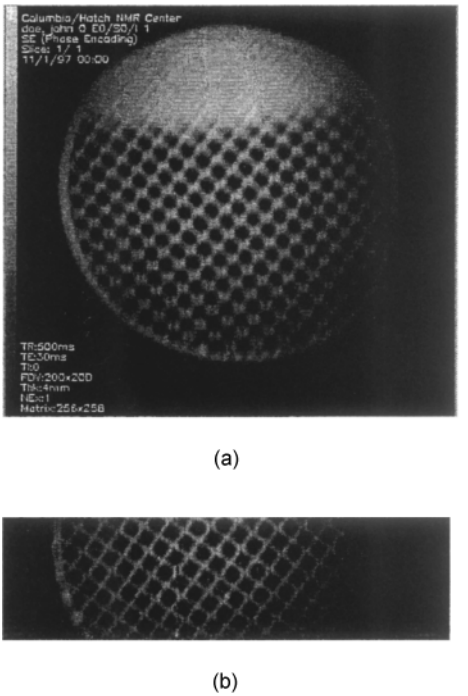

Figure 8 (*a*) Conventional phase encoding. (*b*) Localized wavelet encoding.

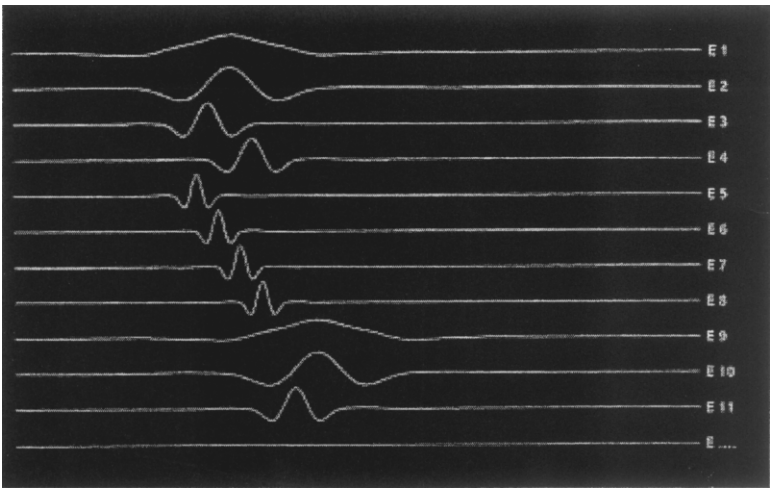

Figure 9 Orthogonal scaling/wavelet functions. E1 shows the scaling functions and E2–E8 are three scales of wavelets. From E9 on, the same but translated set of functions is repeated.

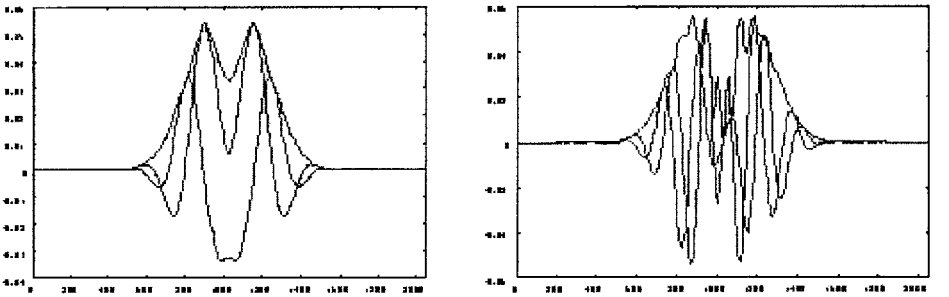

Figure 10 An example of optimized complex scale/wavelet functions.

To achieve optimal noise propagation, the use of a class of complex Daubechies scale/wavelet functions (57) was introduced (EX Wu, J Baude, JM Lina, AF Laine, submitted for publication). For MRI, these functions are easily implemented because of the complex nature of rf excitation pulses. In general, complex wavelet bases were found to yield better noise propagation properties for localized MRI encoding than purely real wavelet bases. A number of complex wavelet bases for optimal noise propagation were designed. They provided an SNR gain factor of 2.5, while still maintaining localized encoding without loss of a practical implementation. In addition to optimization of wavelet basis functions, localized encoding profiles were combined into subgroups in an orthogonal fashion (see Figure 10). This increased the energy under all encoding profiles and thus further increased the SNR without affecting analytical reconstruction (EX Wu, J Baude, JM Lina, AF Laine, submitted for publication). Benefits associated with choosing a set of orthogonal excitation profiles were also described previously (23).

Wavelet Applications in Ultrasound

A fundamental principle used in methods of multiscale denoising and segmentation with wavelet analysis considers a transform domain in which features of interest in a signal can be decorrelated from noise, allowing for a selective reconstruction or segmentation of signal features.

Denoising and Singularity Detection in Doppler Ultrasound Doppler ultrasound echoes from cardiac structures are rich in detail and highly nonstationary. Thus, time-frequency and time-scale analysis are well-suited analytical tools (59). Physiology of the cardiovascular system and heart rate signal is governed by nonlinear chaotic dynamics. Recent studies have shown that an adaptive wavelet denoising method for Doppler ultrasound fetal heart rate (FHR) recordings can isolate deterministic nonlinear structures that were concealed by the noise (60, 61). A complete review of the time-frequency and time-scale analytical tools that have been applied to Doppler ultrasound is offered elsewhere (59). Short-time

Fourier transform, Wigner-Ville transform, wavelet transforms, and model-based time-frequency representations are tested. Their comparison showed little advantage of using logarithmic analysis intervals with a wavelet transform (Hamming wavelets). If only general features of a time-frequency structure are of interest, short-time Fourier transforms or wavelet transform can be used. But, if details of the time-structure are important, components from other time-frequency analytical tools provide superior results.

Another use of Doppler ultrasound is in the detection of small gas bubbles in flowing blood, called microemboli. Ultrasonic recordings from moving microemboli in the middle cerebral artery produce a Doppler-shifted transient reflection. In this case matched-filter detectors that use a wavelet transform produced better results than short-time Fourier transforms (62). Doppler shift signals show a chirping behavior that is caused by acceleration and deceleration of the emboli during their transit through a sample volume. Time-scale chirp detectors provided an overall improvement in detection of $\sim$0.5–0.7 dB.

Tissue Characterization in Cardiac Ultrasound Echoplanar ultrasound is a useful diagnostic tool for imaging organs and soft tissues in the human body. Accurate diagnosis based on tissue visual appearance is very difficult owing to the low resolution of ultrasonic images and the presence of speckle noise. Pathological tissues often reveal changes in their acoustical properties and can be detected by ultrasound as textural patterns with distinct characteristics from normal tissue.

Mojsilovic et al (63, 64) have shown that a scale-frequency method based on separable and nonseparable wavelet transforms is appropriate for the characterization of ultrasonic texture for liver and myocardial tissue. Advantages of a multiscale analysis approach to ultrasound characterization include invariance to gain settings of the transducer, good discrimination of speckle noise in the higher-frequency channels, and powerful assessment of singularities at different scales. In the context of tissue characterization, texture features are extracted via first- and second-order statistics on the analysis coefficients, followed by a binary classification (normal vs diseased). Nonseparable wavelet transforms (65) such as the quincunx transform have been shown to be more robust to noise and less sensitive to rotation than separable wavelet transforms.

Neskovic et al (66) showed that a wavelet-based tissue characterization method applied to 2-D transthoracic ultrasound can differentiate between viable myocardium with recovery potential and myocardial necrosis in the early postinfarction period. In a similar study, Venkatesh (67) showed that the gradient image of multiscale representations can discriminate between healthy and diseased liver.

In most of these studies, feature vectors derived from wavelet-based texture characterization were used with either minimum-distance type classifiers or Bayesian-type classifiers or as neural network inputs for unsupervised classification.

Denoising of Speckle Noise in Ultrasound The formation of ultrasound images under coherent waves results in a granular noisy pattern called speckle. It is caused by the constructive and destructive interference of back-scattered signals owing to tissue inhomogeneity. Speckle noise formation is dependent on the organ tissue property and the orientation of the transducer beam during an acquisition. Speckle noise introduces sharp changes in an image intensity profile. A second artifact, the attenuation artifact, alters the intensity of equally significant structures, depending on their orientation. These artifacts are inherent in the physics of ultrasound and cannot be eliminated during acquisition. Speckle noise significantly degrades image quality, making visual diagnosis difficult and further processing, such as segmentation and edge detection, extremely challenging. Speckle noise reduction techniques include compounding and filtering. The compounding technique averages a series of images of one target at different times (cardiac ultrasound) or for different scanning directions (liver, kidney, . . .). Earlier filtering and denoising techniques include adaptive median filtering (68, 69) and homomorphic Wiener filtering. More recently, Guo et al (70) first reported techniques that use wavelet transforms and thresholding of analysis coefficients before reconstruction. These methods have been widely used for more robust and accurate denoising, because they enable the used to balance noise suppression and signal preservation.

The general framework for methods of wavelet-based denoising is (*a*) computation of multiscale analysis coefficients with a wavelet transform, (*b*) hard or soft thresholding of the coefficients at each scale, and (*c*) reconstruction of the signal via an inverse wavelet transform. Thresholding of the coefficients is aimed at eliminating coefficients that encode noise components (usually in the high frequencies or low scales) and enhancing coefficients that correspond to true signal components (usually in the low frequencies or high scales). Hard thresholding of coefficients resets to zero those coefficients whose magnitude is below a certain threshold, while preserving coefficients above that threshold. Nonlinear thresholding of wavelet coefficients, first introduced by Lai et al (35) and Donoho & Johnstone (71), weights the coefficients with a curve, depending on their magnitude, as illustrated in Figure 11. The basic soft-thresholding operator is defined

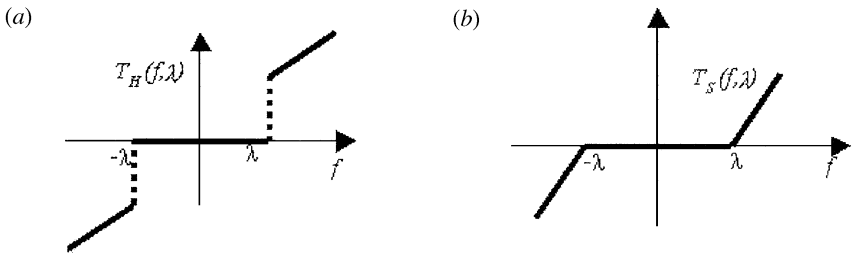

Figure 11 (*a*) Hard-thresholding operator. (*b*) Soft-thresholding operator.

in Equation 9, and the hard-thresholding operators ρ_H with threshold parameter λ applied on signal f are defined below.

$$T_H(f, \lambda) = \begin{cases} f & \text{if } |f| > \lambda \\ 0 & \text{if } |f| \leq \lambda \end{cases} \quad (10)$$

Xiang & Zhang (72) utilized the same threshold across scale, whereas Zong et al (73) selectively applied adaptive denoising and enhancement threshold operators at each scale, by using a sigmoid-shaped weighting curve. They showed that a fine- to coarse-scale space analysis of cardiac B-scan ultrasound on a logarithmic scale could differentiate behaviors of cardiac features from noise. The efficiency of denoising is usually validated by an overall improvement in the consistency of manual tracing of borders by physician experts. Hao & Gao (74) introduced a preprocessing step that separates an original image into two parts—the output of adaptive median filtering and the difference between the original and the filtered image. Both parts are then denoised independently via wavelet thresholding and then recombined to produce the final output. The authors conclude that the combination of adaptive filtering and wavelet coefficient thresholding provides a most effective speckle reduction when compared with single filtering or wavelet analysis alone. Rakotomamonj & Marche (75) recently presented a novel method for lesion enhancement by using a statistical estimator of noise-free signal in a wavelet transform space. ROC analysis has shown that their method performed better than a traditional maximum-likelihood estimator for lesion detection.

Multiresolution Edge Detection Multiresolution edge detection methods have been developed to extract edges at different scales (25, 76–78). Simple multiresolution algorithms include spatial filtering of a fixed image with filters of different sizes or blurring of an image with Gaussian filters of distinct size before edge detection (79, 80). The output of existing multiresolution segmentation is generally a composite edge map that contains edges at multiple scales. Multiresolution segmentation has been extended to wavelet analysis by Mallat et al (25, 81). More recently Boukerroui et al (82, 83) presented an original multiresolution segmentation method on echocardiographic data based on gray-level statistics.

An important issue in multiscale segmentation is the diminution of dimension between the spatial domain and the transform domain, which is caused by the twofold down-sampling in traditional dyadic wavelet analysis. This down-sampling is problematic when manipulating transform coefficients, because there is not a homomorphism between the original signal and coefficient domains. The theory of overcomplete multiscale analysis has been developed to overcome this mathematical limitation. Overcomplete multiscale representations are well suited for image segmentation because they avoid aliasing effects that are introduced by critically sampled representations (3) and that yield a shift invariant representation in which image features are identically localized in both the spatial domain and transform domain. However, overcompleteness is still not always provided in

the multiscale-segmentation methods reported in the literature, and the absence of direct homomorphism between the original and transform spaces can lead to erroneous localization of edges across scales. Obviously in a dyadic framework, interpolation across scale is required for tracking, and there is a lack of mathematics to support the validity of segmentation methods. In another recent work of Setarehdan & Soraghan (84, 85), they present a fuzzy, multiscale edge detection algorithm for ultrasonic data that combines edges at different scales with a fuzzy operator to obtain an optimized tradeoff between detection and localization. Because of the down-sampling at each scale, however, they had to define degrees of edginess for edge point location at each scale.

Phase-based feature extraction methods have also been applied to echocardiographic data (86, 87). In their work, Noble et al showed that, by using log-Gabor wavelet functions, steplike cardiac boundaries could be selectively extracted based on the value of their local phase signature, which is different from the ridgelike structures associated with speckle noise. Nonorthogonal waveletlike Gabor filters have been widely used in biomedical applications (88, 89). The main advantage of phase-based, spatiotemporal ultrasonic edge detection methods is that they are intensity invariant. As mentioned above, tissue attenuation in ultrasound images is position dependent, which makes intensity or gradient-based segmentation methods inappropriate (90–92). A similar approach was presented by Brandt et al (93), which used quadrature filters instead of Gabor-like analytical functions for the segmentation of cardiac boundaries in 2-D + time echocardiographic data.

Computational Anatomy: Automatic Segmentation of Left Ventricular (LV) Volumes from 3-D Cardiac Ultrasound The recent introduction of real-time acquisition via 3-D ultrasound obviates the need for slice registration and reconstruction, leaving segmentation as the remaining barrier to an automated, rapid, and therefore clinically applicable calculation of accurate LV cavity volumes and ejection fractions.

Because it provides such a rich description of the temporal and spatial environment of any area of interest, 3-D ultrasound also offers the potential for increased sensitivity in detecting subtle wall motion abnormality that is indicative of ischemia (e.g. during an exercise stress test), compared with fast MRI techniques. New spatio-temporal segmentation methods that use both spatial and temporal coherence of data are being developed for the extraction of cardiac borders and the reconstruction of beating hearts. Sarti et al (94) presented a nonlinear multiscale analytical method for 3-D echocardiographic data that combines the effect of the regularized Perona-Malik anisotropic diffusion in space (79) and the invariant movie multiscale analysis of Alvarez & Morel (95) in time. This method can filter out the noise component while preserving the coherent space-time structures.

A new spatio-temporal directional analysis tool called the brushlet, first introduced by Meyer & Coifman in 1997 (16), has been shown to be remarkably effective in the analysis of ultrasound data. Angelini et al (96) developed directional denoising and segmentation in three dimensions for feature extraction,

by identifying efficient brushlet projection coefficients within sets of redundant articulated (orientation-rich) bases. An example of a set of coefficients for an overcomplete transform in 12 different directions is displayed in Figure 12.

Clinical cardiac volumes were analyzed with the brushlet basis for tiling of the Fourier domain in 64 cubes with overcomplete representations. This analysis provided a decomposition of four brushstrokes, which were represented by paired diagonal cubes. The brushstroke orientation in each of the three directions was $\pm 45^\circ$ for each cube.

Visualization in 3-D used isosurfaces and isovolumes at selected levels. The level was set as the maximum value of each gradient volume in the transform domain. The "marching cube" algorithm (96a) was used for the isovolume computation. Results that are displayed in Figure 13 showed the ability of the transform domain to isolate dynamical information from the filling of the LV cavity and the position of the papillary muscles during the entire cardiac cycle.

Wavelets in Tomographic Reconstruction

The radon transform is the mathematical basis of positron emission tomography imaging, computer tomography, and single positron emission computerized tomography imaging. In two dimensions, the radon transform is equivalent to the X-ray transform and is defined by

$$\mathcal{R} f(\alpha, s) = \int_{x \in \mathbb{R}^2, x.\alpha = 0} f(x + s\alpha)\, dx \quad \text{for } \alpha \in \mathbb{S} \quad \text{and} \quad s \in \mathbb{R} \qquad (11)$$

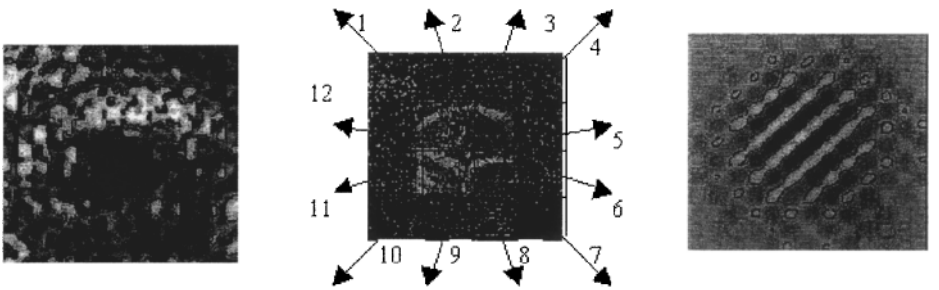

(*a*) (*b*) (*c*)

Figure 12 (*a*) Original cardiac ultrasound slice (64 × 64 pixels) from four-dimensional data. (*b*) Real part of coefficients for a 16-quadrant tiling (4 × 4 × 4 tiling in $x \times y \times z$ directions) of the Fourier plane. A total of 12 distinct directions are covered by the 16 quadrants in the $(x - y)$ plan. In the overcomplete framework, each coefficient quadrant has the same dimension as the original image matrix. (*c*) A 2-D brushlet basis function for a particular direction and frequency. The direction is determined by the position of the quadrant in the Fourier plan. The frequency of the brushlet basis function, equivalent to the resolution of the brushlet basis, is determined by the size of the quadrant in the Fourier plan.

Figure 13 Visualization of 3-D volume of left-ventricular cavity in time for one cardiac cycle. (*a*, *b*) Systolic phase (ejection of blood from the left ventricle). (*c*, *d*) Diastole phase (filling of blood from right atrium to right ventricle).

where $\mathbb{S}$ is the unit circle. For a detailed presentation of the radon transform and its properties, we refer the reader elsewhere (97).

Inverting the radon transform is necessary to reconstruct images from tomographic data. However, this inverse problem is ill-posed, because the radon transform acts as a smoothing transform whose inverse is unbounded and because the observed data Y are always in practice contaminated by a perturbation error in the observation process, which can be modeled as an additive noise Z:

$$Y = \mathcal{R}f + Z \tag{12}$$

When applying the inverse $\mathcal{R}^{-1}$ of the radon transform to the observed data Y, the noise value $\mathcal{R}^{-1}Z$ becomes large, and the quality of the reconstructed image is poor, which suggests that the problems of tomographic data denoising and tomographic data reconstruction are completely intertwined. The classical regularization procedures to solve this inverse problem are linear-filtering methods and the most popular approach, filtered back projection (FBP), which is computed by an iterative algorithm.

First studies of the relations between wavelet transforms and the radon transform were conducted by Holschneider (98) and Walnut (99) to derive radon inversion schemes. Peyrin et al (100) showed that a 2-D wavelet transform of the tomographic image can be constructed from the wavelet transform of its projections. Many researchers have rapidly developed various wavelet-based tomographic

reconstruction techniques that are basically combinations of a discrete or a continuous 1-D wavelet transform of the projection data with linear FBP (101–108). The main concern underlying these approaches is local reconstruction. Bhatia et al (109) combined this type of approach with an MAP model, using a quadratic regularization of the 1-D projection data (109). In another paper (110), the 1-D projection data were back-projected on a different basis to derive a sparse formulation of the problem, using again a maximum a posteriori (MAP) model of the image.

A 2-D wavelet decomposition in the image domain has also proven to be a valuable tool for tomographic reconstruction. Delaney & Bresler (111) have studied its use to implement a numerically efficient classical FBP algorithm, and it has also been used to implement Tikhonov's regularization methods in different regularity spaces such as Sobolev spaces (112) and Besov spaces (N Lee & B Lucier, submitted for publication).

Sahiner & Yagle (114) and Olson (115) have investigated the use of the wavelet transform to solve the limited-angle tomographic reconstruction problem, when projection data are missing over a range of angles.

The use of wavelets in tomographic reconstruction is justified by two properties of wavelets; they are adapted both to the behavior of the operator to be inverted and to the type of signals one wants to recover. That is, if one chooses orthogonal wavelets of sufficient regularity and with enough vanishing moments, the radon transform operator is nearly diagonal in the orthogonal basis. But, in contrast to the Fourier basis, which is used in linear-filtering reconstruction methods, the wavelet basis also provides a compact representation of spatially heterogeneous data such as medical images and, in that sense, also provides a diagonalization of prior information on medical images. The work of David Donoho on the use of a wavelet-vaguelette decomposition (WVD) for the inversion of the radon transform is based on these two ideas (116).

In the WVD approach, the function f to be recovered is decomposed in a wavelet basis

$$f = \sum_{j,k} \langle f, \psi_{j,k} \rangle \psi_{j,k} \tag{13}$$

Let us denote $\Psi_{j,k} = \mathcal{R}\psi_{j,k}$. Donoho showed that there exist constants $\beta_{j,k}$ such that the family of scaled functions $(\Psi_{j,k}/\beta_{j,k})_{j,k}$ is a Riesz basis of the range $R(\mathcal{R})$ of the radon transform and, for any $f \in L^2(\mathbb{R}^2)$, the WVD is defined by

$$f = \sum_{j,k} c_{j,k} \langle \mathcal{R} f, \Psi_{j,k}/\beta_{j,k} \rangle \psi_{j,k} \tag{14}$$

where $(c_{j,k})_{j,k}$ are known scalars.

The WVD can be viewed as a nonlinear wavelet-based analog of the windowed singular value decomposition (windowed SVD) approach, defined as follows: let $\mathcal{R}^*$ be the adjoint operator of $\mathcal{R}$. $\mathcal{R}^*\mathcal{R}$ is a compact operator, whose eigenfunctions

and eigenvalues are respectively denoted e_n and k_n, and let h_n be the normalized image $h_n = \frac{\mathcal{R}e_n}{||\mathcal{R}e_n||}$. If none of the eigenvalues k_n is zero, the SVD is defined by

$$f = \sum_n k_n^{-1} \langle \mathcal{R} f, h_n \rangle e_n \tag{15}$$

Because the eigenvalues of $\mathcal{R}^*\mathcal{R}$ tend to zero, we define the windowed SVD by picking weights w_n close to 1 for n small and close to 0 for n large, and we obtain the windowed SVD estimator

$$\tilde{f} = \sum_n w_n k_n^{-1} \langle Y, h_n \rangle e_n \tag{16}$$

The windowed SVD encompasses, in its theoretical definition, many linear approaches (117); linear FBP is actually a windowed SVD estimator for special values of w_n, as is Tikhonov's quadratic-regularization method. Moreover, it has been proven that the windowed SVD can provide a linear estimator that is optimal in a minimax sense among all linear estimators (118, 119). A minimax estimator is an estimator that minimizes the worst case risk over a set Θ

$$\sup_{f \in \Theta} E || \tilde{f} - f ||_2^2 \tag{17}$$

where $\tilde{f}$ is the estimate of f and Θ is a smoothness set in which we incorporate our prior information on f and in which f is guaranteed to belong. Examples of sets Θ for minimax estimation are Sobolev spaces, Besov spaces, and bounded variation sets.

The SVD is a generic formulation of linear estimation to solve inverse problems. As a linear technique, its limitations come from the fact that the basis functions of a SVD derive completely from the operator to be inverted, in our case the radon transform, and do not incorporate the physical properties of signals. However, it is essential that the signal be represented by only a few significant coefficients in the basis functions.

The nonlinear WVD approach responds to the limitations of SVD, because it efficiently represents both the radon transform and the prior information on spatial inhomogeneous regularity of a signal. To perform a tomographic reconstruction in the presence of noisy data, the WVD can be combined with a wavelet shrinkage method, which attenuates the wavelet coefficients of the acquired data by a certain amount toward zero. Donoho (116) showed that a WVD is optimal in a minimax sense among all linear and nonlinear estimators for inverting certain types of homogeneous linear operators, including the radon transform, and the minimax rate of convergence for a quadratic loss is faster than the rate of convergence of SVD or any linear procedure.

Kolaczyk (120) has numerically investigated the use of a WVD for tomographic reconstruction, whereas Abramovich & Silverman have theoretically and numerically studied variants of the WVD (121). Very recently, N Lee & B Lucier (submitted for publication) have refined the theoretical results and the numerical approach

for computing WVD, showing that the WVD method is equivalent to minimizing a variational formulation with Besov norms. The corresponding experimental results exhibit significant improvements over FBP methods.

Wavelets in Digital Mammography: Enhancement and Mass Detection

Wavelets are an attractive analytic tool for accomplishing contrast enhancement and detection of masses in mammograms, because of the arbitrary shapes and variable sizes of mammographic findings (typically from a few millimeters to a centimeter). Multiscale methods have achieved remarkable results when compared with traditional single-scale techniques in applications of contrast enhancement (122) and detection of subtle masses (123).

The principal insight in applications of digital radiographs is that diagnostic features, such as masses, microcalcifications, and spicular lesions in mammograms, can be characterized at some distinct scale in a space-frequency representation, whereas noise and other structures are attenuated or discarded. Contrast enhancement algorithms have relied on overcomplete multiscale representations (124–129). As mentioned above, overcomplete multiscale representations are desirable for image enhancement, because they avoid aliasing effects that are introduced by critical sampling (54) and they yield a shift invariant representation. Figure 14 shows an example for one level of an overcomplete wavelet decomposition of a spiculated mass. Modification of these coefficients can result in more informative diagnostic images with enhanced features and an increased SNR without introducing any local distortions or artifacts (130).

Enhancement of coefficients has been carried out via adaptive nonlinear operators. However, optimal selection of multiscale basis functions, levels of analysis, gain/attenuation functions, and parameters needs to be further validated for clinical soft-copy display platforms. Optimization of contrast enhancement protocols by using mathematical models has been carried out via image quality assessment with quantitative measures such as SNR and contrast improvement index (131). Below, we review some of the more recent work done in this area of medical imaging.

Computer-Assisted Diagnostic Systems for Mammography Screening Mammography screening is recognized as the most reliable method for the early

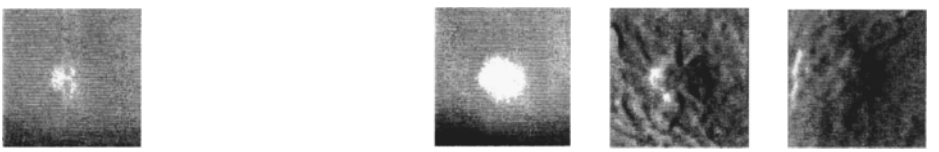

Figure 14 Level 5 of an overcomplete dyadic wavelet decomposition of a spiculated mass. *Left to right*: original image, approximation image, horizontal details, and vertical details.

detection of breast cancer. Diagnosis with mammograms is based on reading of radiographs, which requires visualization of subtle breast tissues combined with knowledge of anatomical structures and physiology of the breast.

It has been reported that negative mammograms were observed in 10%–30% of the women who actually have breast cancer (132, 133). Approximately 40% of these misdiagnosed cancers appear as masses on the mammograms (133) on postreview. CAD for mammography screening has been developed as a "second opinion" or as a "prereader," which prompts attention to suspicious regions, for example, drawing the attention of radiologists to a tumor that they might otherwise have overlooked (124, 134, 135). The general approach of CAD schemes is (*a*) image preprocessing, normally aided by contrast enhancement, (*b*) segmentation of the suspicious region, and (*c*) feature description and classification within a marked region. The detection of malignant masses is more challenging because benign masses and other types of lesions have similar radiographic densities and a variety of sizes (123). Wavelet transforms, providing the capability to analyze features over different scales, have been the method of choice for feature enhancement and detection algorithms that support CAD systems (57, 122, 136–139).

Enhancement of Mammographic Features by Multiscale Analysis Most radiographic films provide about 256 gray levels of contrast resolution. However, computed imaging modalities with digital detectors can acquire at least 1024 distinct levels of gray. There is a wealth of dynamic range within these digital images. However, expert radiologists can detect at most 128 shades of gray. This large disparity between sensor resolution and human perception has motivated the development of image-processing methods that can "data mine" these rich images and present information within the range of gray scale levels that is perceivable to the human eye.

Multidimensional feature enhancement via wavelet analysis has been previously demonstrated and implemented on mammograms (130, 140, 141) and appears to be a promising tool for processing digital medical images. Further results are presented elsewhere (142–144, 146–149). In most of these papers, the enhancement process acts on wavelet coefficients at some particular spatial-frequency scale by boosting, decreasing, or resetting their values. The image is then reconstructed with the modified coefficients. This simple enhancement technique relies on the idea that features of interest in a given image are detectable at a particular scale space, whereas noise and less significant structures may live at other levels of analysis whose influence can be diminished or eliminated in a reconstructed image.

Previous studies have shown that multiscale analysis is very well adapted for enhancement of medical images (5, 59). For example, improvement of the contrast index in a region of a mammogram containing a subtle mass has been described in detail (122). The image was analyzed with biorthogonal wavelet functions for three levels and then reconstructed.

Laine & Song (136) first demonstrated nonlinear enhancement of mammograms by adaptively weighting the details computed by using a first derivative

of a Gaussian wavelet. In later work (137), analysis with a dyadic wavelet and linear weights was shown to be equivalent to unsharp masking at multiple scales. Given the arbitrary sizes and shapes of biological structures, continuous scale representations (142) can provide more flexibility compared with analytic methods computed at dyadic scales. Lu & Healy (138) used a multiscale edge representation to achieve contrast enhancement. Other types of wavelets have been applied, such as complex Daubechies wavelets (57), and wavelet packets (139). An example of using global enhancement by multiscale adaptive gain processing (142) is shown below in Figure 15.

Detection and Classification of Masses in Mammograms In the research of Patrick et al (150, 151), a wavelet transform was used to decompose regions of interest into several scales, from which multiresolution texture features were calculated from the corresponding original images and the wavelet coefficients at each level. A linear discriminant classifier was then used to identify masses within the mammogram. Qian et al (152–154) used a directional wavelet transform, which provided a preprocessing step for segmentation of suspicious areas, to extract morphologic and directional features. In their research, adaptive methods of parameter selection were proposed for feature enhancement. A wavelet-driven feature extraction scheme based on a Gaussian Markov random-field model for mammographic images has also been investigated (155, 156). Adaptive features based on the nonstationary assumption of a Gaussian Markov nonrandom field were defined for each pixel of the mammogram, and then segmentation by a fuzzy C-means algorithm was applied to localize mammographic findings. In addition, multiscale statistical analytical methods that are based on image probability density functions

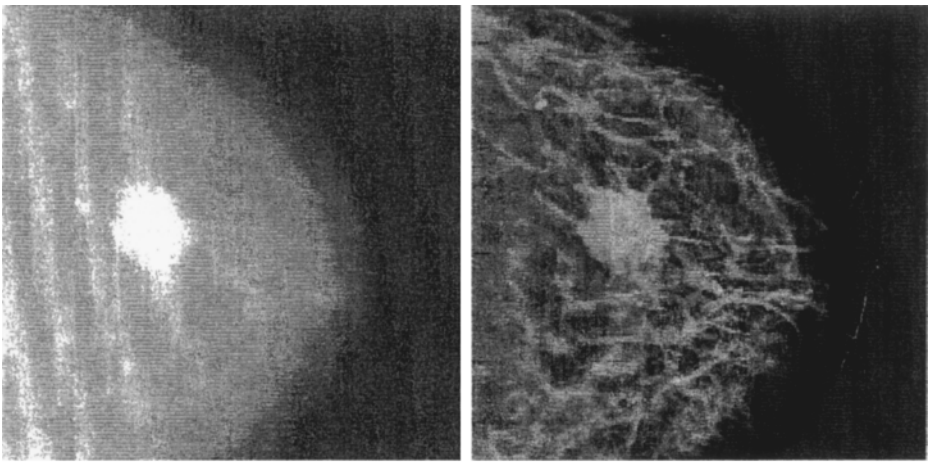

Figure 15 (*a*) Original mammogram containing a mass lesion. (*b*) Enhanced mammogram showing well-defined borders of the mass and clarity of subtle breast tissue and structures.

(157) and maximum entropy (158) have also been reported in the literature. Finally, automated detection and classification of masses have been accomplished by methods of template matching (159) and artificial neural networks (160, 161). The range and variety of multiscale bases available for image analysis are very wide and diversified. However, little work has been done to systematically select the best basis for accomplishing enhancement and detection of masses (122, 162, 163).

ACKNOWLEDGMENTS

The author credits Jerome Kalifa, Elsa Angelini, Ralf Mekle, and Yinpeng Jin for their outstanding efforts in researching the application areas reviewed in this article. In addition, the author expresses his sincere appreciation to Professor Ingrid Daubechies for her encouragement and inspiration of this manuscript.

LITERATURE CITED

1. Vetterli M, Kovacevic J. 1995. *Wavelets and Subband Coding*. Englewood Cliffs, NJ: Prentice-Hall
2. Strang G, Nguyen T. 1996. *Wavelets and Filter Banks*. Boston: Wellesley-Cambridge
3. Mallat S. 1999. *A Wavelet Tour of Signal Processing*. New York: Academic. 2nd ed.
4. Daubechies I. 1992. *Ten Lectures on Wavelets*. Philadelphia: Soc. Indust. Appl. Math.

4a. Aldroubi A, Unser M, eds. 1996. *Wavelets in Medicine and Biology*, p. 378. Boca Raton, FL: CRC Press. 378 pp.

5. Unser M, Aldroubi A. 1996. A review of wavelets in biomedical applications. *Proc. IEEE* 84:626–38
6. Unser M. 1996. Wavelets, statistics and biomedical applications. In *IEEE Signal Process. Workshop Stat. Signal Array Process., 8th, Corfu, Greece*, Los Alamitos, CA: IEEE Comp. Soc.
7. Meyer Y. 1993. *Wavelets: Algorithms and Applications*. Philadelphia: SIAM. 450 pp.
8. Cohen A, Daubechies I, Feauveau J. 1992. Biorthogonal bases of compactly supported wavelets. *Commun. Pure Appl. Math.* 45:485–560
9. Alpert B, Rokhlin V. 1991. A fast algorithm for the evaluation of legendre expansions. *SIAM J. Sci. Stat. Comput.* 12:158–73
10. Geronimo J, Hardin D, Massopast PR. 1994. Fractal functions and wavelet expansions based on several functions. *J. Approx. Theory* 78:373–401
11. Strang G, Strela V. 1995. Short wavelets and matrix dilation equations. *IEEE Trans. Signal Proc.* 43:108–15
12. Cohen A, Daubechies I, Vial P. 1993. Wavelet bases on the interval and fast algorithms. *J. Appl. Comput. Harmonic Anal.* 1:54–81
13. Sweldens W. 1997. The lifting scheme: a construction of second generation wavelets. *SIAM J. Math. Anal.* 29:511–46
14. Sweldens W, Schröder P. 1996. Building your own wavelets at home. In *Wavelets in Computer Graphics*, pp. 15–87. New York: ACM SIGGRAPH, Addison Wesley
15. Coifman R, Donoho D. 1995. *Translation invariant de-noising. Tech. Rep. 475*. Stanford, CA: Stanford Univ. Dep. Stat.
16. Meyer F, Coifman RR. 1997. Brushlets: a tool for directional image analysis and image compression. *Appl. Comp. Harmonic Anal.* 4:147–87
17. Freeman W, Adelson E. 1991. The design

and use of steerable filters. *IEEE Trans. Pattern Anal. Mach. Intell.* 13:891–906
18. Malvar HS. 1988. The LOT: a link between block transform coding and multirate filter banks. In *Proc. IEEE Int. Symp. Circuits Syst., Espoo, Finland, June*, pp. 835–38. IEEE Press
19. Coifman R, Meyer Y. 1991. Remarques sur l'analyse de Fourier a fenêtre. *C.R. Acad. Sci.* 312:259–61
20. Wickerhauser MV. 1994. *Adapted Wavelet Analysis from Theory to Software*. Wellesley, MA: AK Peters
21. Auscher P, Weiss G, Wickerhauser M. 1992. Local sine and cosine bases of Coifman and Meyer and the construction of smooth wavelets. In *Wavelets: A Tutorial in Theory and Applications*, ed. C Chui, pp. 237–56. New York: Academic
22. Coifman R, Wickerhauser M. 1992. Entropy-based algorithms for best basis selection. *IEEE Trans. Inf. Theory* 38(2): 713–18
23. Healy D, Weaver J. 1992. Two applications of wavelet transforms in magnetic resonance imaging. *IEEE Trans. Inf. Theory* 38(2):840–60
24. Healy D, Lu J, Weaver J. 1995. Two applications of wavelets and related techniques in medical imaging. *Ann. Biomed. Eng.* 23:637–65
25. Mallat S, Zhong S. 1992. Characterization of signals from multiscale edges. *IEEE Trans. Pattern Recognit. Mach. Intell.* 14(7):710–32
26. Mallat S. 1991. Zero-crossings of a wavelet transform. *IEEE Trans. Inf. Theory* 37(4): 1019–33
27. Nowak R. 1998. Wavelet-based Rician noise removal for magnetic resonance imaging. *IEEE Trans. Image Proc.* 8:1408–19
28. Macovski A. 1996. Noise in MRI. *Magnet. Reson. Med.* 36:494–97
29. Gudbjartsson H, Patz S. 1995. The Rician distribution of noisy MRI data. *Magn. Reson. Med.* 34:910–14
30. Ogawa S, Lee T, Nayak A, Glynn P. 1990. Oxygenation-sensitive contrast in magnetic resonance image of rodent brain at high magnetic fields. *Magn. Reson. Med.* 14:68–78
31. Moonen CTW. 1995. Imaging of human brain activation with functional MRI. *Biol. Psychiatry* 37:141–43
32. Hajnal JV, Myers R, Oatridge A, Schwieso JE, Young IR, Bydder GM. 1994. Artifacts due to stimulus correlated motion in functional imaging of the brain. *Magn. Reson. Med.* 31:283–91
33. Duyn JH, Moonen CT, van Yperen GH, de Boer RW, Luyten PR. 1994. Inflow versus deoxyhemoglobin effects in functional MRI using gradient echos at 1.5 T. *NMR Biomed.* 7:83–88
34. Kim SG, Hendrich K, Hu XP, Merkle H, Ugurbil K. 1994. Potential pitfalls of functional MRI using conventional gradient-recalled echo techniques. *NMR Biomed.* 7:69–74
35. Lai S, Hopkins AL, Haacke EM, Wasserman DA, Buckley P, et al. 1993. Identification of vascular structures as a major source of signal contrast in high resolution 2-d and 3-d functional activation imaging of the motor cortex at 1.5 t. *Magn. Reson. Imaging* 30:387–92
36. Hilton M, Odgen T, Hattery D, Eden G, Jawerth J. 1996. Wavelet denoising of functional MRI data. See Ref. 164, pp. 93–114
37. Donoho D, Johnstone I. 1994. Ideal spatial adaptation via wavelet shrinkage. *Biometrika* 81:425–55
38. Donoho DL. 1995. De-noising by soft-thresholding. *IEEE Trans. Inf. Theory* 41: 613–27
39. Ruttimann UE, Unser M, Rawlings RR, Rio D, Ramsey NF, et al. 1998. Statistical analysis of functional MRI data in the wavelet domain. *IEEE Trans. Med. Imaging* 17:142–54
40. Fu Z, Hui Y, Liang ZP. 1998. Joint spatiotemporal statistical analysis of functional MRI data. In *Int. Conf. Image*

Process. ICIP98, pp. 709–13. *Chicago, IL*. Los Alamitos, CA: IEEE Press
41. Brammer MJ. 1998. Multidimensional wavelet analysis of functional magnetic resonance images. *Hum. Brain Mapp.* 6: 378–82
42. Weaver JB. 1998. Monotonic noise suppression used to improve the sensitivity of fMRI activation maps. *J. Digit. Imaging* 11:46–52
43. Kok CW, Hui Y, Nguyen TQ. 1997. MRI truncation artifact reduction via wavelet shrinkage. In *Wavelet Applications IV, Orlando, FL*.
44. Wolstenhome CBH, Taylor CJ. 1999. Wavelet compression of active appearance models. In *Med. Imaging Comput.-Assist. Intervention—MICCAI'99, Cambridge, UK*. pp. 544–54. Berlin: Springer-Verlag
45. Boom H, Robinson C, Rutten W, Neumann M, Wijkstra H. 1997. Improved t2 and diffusion maps from wavelet denoised magnetic resonance imaging. In *Ann. Int. Conf. IEEE Eng. Med. Biol. Soc. Amsterdam*
46. Baskurt A, Peyrin F, Benoit-Catin H, Goutte R. 1993. Coding of 3d medical images using 3d wavelet decompositions. In *IEEE Int. Conf. Acoust., Speech, Signal Process., ICASSP-93. Minneapolis, MN*, pp. 562–65. New York: IEEE Press
47. Pratt MA, Chu CH, Wong S. 1996. Volume compression of MRI data using zerotrees of wavelet coefficients. In *Wavelet Appl. Signal Image Process. IV, Denver, CO*
48. Chwialkowski MP, Ibrahim YM, Li HF, Peshock RM. 1996. A method for fully automated quantitative analysis of arterial flow using flow-sensitized MR images. *Comput. Med. Imaging Graph.* 20:365–78
49. Yu TPY, Stoschek A, Donoho DL. 1996. Translation- and direction-invariant denoising of 2-d and 3-d images: experience and algorithms. In *Wavelet Appl. Signal Image Process. IV, Denver, CO*
50. Weaver JB, Yansun X, Healy DM, Driscoll JR. 1992. Wavelet-encoded MR imaging. *Magn. Reson. Med.* 24:275–87
51. Panych LP, Jakab PD, Jolesz FA. 1993. Implementation of wavelet-encoded MR imaging. *J. Magn. Reson. Imaging* 3:649–55
52. Panych LP, Jolesz FA. 1994. A dynamically adaptive imaging algorithm for wavelet-encoded MRI. *Magn. Reson. Med.* 32:738–48
53. Gelman N, Wood ML. 1996. Wavelet encoding for 3-d gradient-echo MR-imaging. *Magn. Reson. Med.* 36:613–19
54. Mallat S. 1989. A theory for multiresolution signal decomposition: the wavelet representation. *IEEE Trans. Pattern. Recognit. Mach. Intell.* 11(7):674–93
55. Wu EX, Laine AF, DeLaPaz RL, Alderson OP. 1998. General optimization of wavelet encoding for practical MRI and implementation on a high field system. In *Proc. Magn. Reson. Med. 6th Sci. Meet., Sydney, Aust*.
56. Kyriakos WE, Panych LP. 1997. In *Book of Abstracts*. Soc. Magn. Reson. Med.
57. Lina JM, Mayrand M. 1996. Complex Daubechies wavelets. *J. Appl. Comput. Harmonic Anal.* 2:219–29
58. Deleted in proof
59. Akay M, ed. 1998. *Time Frequency and Wavelets in Biomedical Signal Processing*. Piscataway, NJ: IEEE Press
60. Papadimitriou S, Gatzounas D, Papadopoulos V, Tzigounis V, Bezerianos A. 1997. Time-scale detection of microemboli in flowing blood with doppler ultrasound. *IEEE Trans. Biomed. Eng.* 53: 177–269
61. Papadimitriou S, Bezerianos A. 1999. Nonlinear analysis of the performance and reliability of wavelet singularity detection based denoising for doppler ultrasound fetal heart rate signals. *Int. J. Med. Inf.* 53:43–60
62. Krongold BS, Sayeed AM, Moehring MA, Ritcey JA, Spencer MP, Jones DL. 1999. Time-scale detection of microemboli in flowing blood with Doppler ultrasound. *IEEE Trans. Biomed. Eng.* 46:1081–90

63. Mojsilovic A, Popovic MV, Neskovic AN, Popovic AD. 1997. Wavelet image extension for analysis and classification of infarcted myocardial tissue. *IEEE Trans. Biomed. Eng.* 44:856–66
64. Mojsilovic A, Popovic M, Markovic S, Krstic M. 1998. Characterization of visually similar diffuse diseases from b-scan liver images using nonseparable wavelet transform. *IEEE Trans. Med. Imaging* 17: 541–50
65. Kovačević J, Vetterli M. 1992. Nonseparable multidimensional perfect reconstruction filter banks and wavelet bases for $\mathcal{R}^n$. *IEEE Trans. Inf. Theory* 38(2):533–55
66. Neskovic AN, Mojsilovic A, Jovanovic T, Vasiljevic J, Popovic M, et al. 1998. Myocardial tissue characterization after acute myocardial infarction with wavelet image decomposition: a novel approach for the detection of myocardial viability in the early postinfarction period. *Circulation* 18:634–75
67. Venkatesh YV. 1996. A generalized hermite pyramid for ultrasonic image analysis. *Ultrason. Imaging* 18:261–304
68. Loupas T, McDicken WN, Allan PL. 1989. An adaptive weighted median filtering for speckle suppression in medical ultrasonic images. *IEEE Trans. Circuits Syst.* 36:129–35
69. Karaman M, Kutay A, Bodgazi G. 1995. An adaptive speckle filter for medical ultrasonic imaging. *IEEE Trans. Med. Imaging* 14:283–93
70. Guo H, Odegard JE, Lang M, Gopinath RA, Selesnick IW, Burrus CS. 1994. Wavelet based speckle reduction with application to SAR based ATD/R. In *IEEE Int. Conf. Image Process*. 1:75–79. Los Alamitos, CA: IEEE Comput. Soc.
71. Donoho D, Johnstone I. 1994. Threshold selection for wavelet shrinkage of noisy data. In *Ann. Int. Conf. IEEE Eng. Med. Biol. Soc., 16th*, 1:A24–25. Los Alamitos, CA: IEEE Press
72. Xiang SH, Zhang YT. 1996. Maximization of the signal-to-noise ratio for two dimensional medical ultrasound transducer sensitivity improvement by denoising wavelets. In *Int. Conf. Biomed. Eng., Hong Kong*
73. Zong XL, Laine AF, Geiser EA. 1998. Speckle reduction and contrast enhancement of echocardiograms via multiscale nonlinear processing. *IEEE Trans. Med. Imaging* 17:532–40
74. Hao X, Gao S. 1999. A novel multiscale nonlinear thresholding method for ultrasonic speckle suppressing. *IEEE Trans. Med. Imaging* 18:787–94
75. Rakotomamonj A, Marche P. 1998. Wavelet-based enhancement of lesion detectability in ultrasound b-scan images. In *Ann. Conf. IEEE Eng. Med. Biol. Soc., 20th, Hong Kong*, pp. 808–11
76. Bergholm F. 1987. Edge focusing. *IEEE Trans. Pattern Anal. Mach. Intell.* 9:726–41
77. Schrift A, Zeevi Y, Porat M. 1988. Pyramidal edge detection and image representation. In *SPIE Vis. Comm. image Proc., Cambridge, MA*, pp. 529–36
78. Park DJ, Nom K, Park RH. 1980. Multiresolution edge detection technique. *J. Korean Inst. Telematics Electron.* 288(12)
79. Perona P, Malik J. 1990. Scale-space and edge detection using anisotropic diffusion. *IEEE Trans. Pattern. Anal. Mach. Intell.* 12:629–39
80. Canny J. 1986. A computational approach to edge detection. *IEEE Trans. Pattern Recognit. Mach. Intell.* 36:961–1005
81. Mallat S, Hwang WL. 1992. Singularity detection and processing with wavelets. *IEEE Trans. Inf. Theory* 38(2):617–43
82. Boukerroui D, Basset O, Guerin N, Baskurt A. 1998. Multiresolution texture based adaptive clustering algorithm for breast lesion segmentation. *Eur. J. Ultrasound* 8: 135–44
83. Boukerroui D, Basset O, Baskurt A, Noble A. 1990. Segmentation of echocardiographic data. multiresolution 2d and 3d algorithm based on grey level statistics. In

MICCAI'99. Cambridge, UK, pp. 516–23. Berlin: Springer-Verlag

84. Setarehdan SK, Soraghan JJ. 1999. Automatic cardiac LV boundary detection and tracking using hybrid fuzzy temporal and fuzzy multiscale edge detection. *IEEE Trans. Biomed. Eng.* 46:1364–78
85. Setarehdan SK, Soraghan JJ. 1999. Fuzzy multiscale edge detection (FMED) applied to automatic left ventricle boundary extraction. In *Int. Conf. Image Process. Appl. 7th, Manchester, UK*, 2:552–56
86. Jacob G, Noble JA, Mulet-Parada M, Blake A. 1999. Evaluating a robust contour tracker on echocardiographic sequences. *Med. Image Anal.* 3:63–75
87. Mulet-Parada M, Noble JA. 1998. 2D+T acoustic boundary detection in echocardiography. In *Med. Image Comput. Comput.-Assist. Interv.—MICCAI'98, Boston, MA*, pp. 806–13. Berlin: Springer-Verlag
88. Porat M, Zeevi Y. 1988. The generalized Gabor scheme of image representation in biological and machine vision. *IEEE Trans. Pattern Recognit. Mach. Intell.* 10(4):452–68
89. Porat M, Zeevi Y. 1989. Localized texture processing in vision: analysis and synthesis in Gaborian space. *IEEE Trans. Biomed. Eng.* 36(1):115–29
90. Adam D, Hareuveni O, Sideman S. 1989. Semiautomated border tracking of cine echocardiographic ventricular images. *IEEE Trans. Med. Imaging* 6:266–71
91. Chu CH, Delp EJ, Buda AJ. 1988. Detecting left ventricular endocardial and epicardial boundaries by digital two-dimensional echocardiography. *IEEE Trans. Med. Imaging* 7:81–90
92. Linker DT, Pearlman AS, Lewellen TK, Huntsman LH, Moritz WE. 1982. Automatic endocardial definition of 2-D echocardiograms: a comparison of four standard edge detectors and improved thresholding techniques. In *Computers in Cardiology*, pp. 395–38. New York: IEEE Press
93. Brandt E, Wigstrom L, Wranne B. 1999. Segmentation of echocardiographic image sequences using spatiotemporal information. In *MICCAI'99, Cambridge, UK*, pp. 410–19. Berlin: Springer-Verlag
94. Sarti A, Mikula K, Sgallari F. 1999. Nonlinear multiscale analysis of three-dimensional echocardiographic sequences. *IEEE Trans. Med. Imaging* 18:453–66
95. Alvarez L, Morel JM. 1994. Formalization and computational aspects of image analysis. *Acta Numer.* 1–59
96. Angelini E, Laine A, Takuma S, Homma S. 1999. Directional representations of 4d echocardiography for temporal quantification of LV volumes. In *Med. Imaging Comput. Comput.-Assist. Interv.—MICCAI'99, Cambridge, UK*, pp. 430–40. Berlin: Springer-Verlag

96a. Lorensen WE, Cline HE. 1987. Marching Cubes: a high resolution 3D surface construction algorithm. *Comput. Graph.* 21:163–69

97. Deans S. 1983. *The Radon Transform and Some of Its Applications*, 289 pp. New York: Wiley & Sons
98. Holschneider M. 1991. Inverse Radon transforms through inverse wavelet transforms. *Inverse Probl.* 7:853–61
99. Walnut D. 1992. Applications of Gabor and wavelet expansions to the Radon transform. In *Probabilistic and Stochastic Methods in Analysis with Applications*, ed. JS Byrnes, pp. 187–205. Boston: Kluwer Acad.
100. Peyrin F, Zaim M, Goutte R. 1993. Construction of wavelet decompositions for tomographic images. *J. Math. Imaging Vis.* 3:105–21
101. Berestein C, Walnut D. 1996. Wavelets and local tomography. See Ref. 4a, pp. 231–58
102. Olson T, DeStefano J. 1994. Wavelet localization of the Radon transform. *IEEE Trans. Image Proc.* 42:2055–67
103. Olson T. 1995. Optimal time-frequency projections for localized tomography. *Ann. Biomed. Eng.* 23:622–836

104. Rashid-Farrokhi F, Liu K, Berenstein C, Walnut D. 1997. Wavelet-based multiresolution local tomography. *IEEE Trans. Image Proc.* 22:1412–30
105. Zhao S, Wang G, Hsieh J. 1997. Wavelet sampling and localization schemes for the Radon transform in two dimensions. *SIAM J. Appl. Math.* 57:1749–62
106. Bottema M, Moran B, Suorova S. 1998. An application of wavelets in tomography. *Digit. Signal Process.* 8:244–54
107. Maldych W. 1999. Tomography, approximate reconstructions, and continuous wavelet transforms. *J. Appl. Comput. Harmonic Anal.* 7:54–100
108. Zhao S. 1999. Wavelet filtering for filtered backprojection in computer tomography. *J. Appl. Comput. Harmonic Anal.* 6:346–73
109. Bhatia M, Karl W, Willsky A. 1996. A wavelet-based method for multiscale tomographic reconstruction. *IEEE Trans. Med. Imaging* 15:92–101
110. Bhatia M, Karl W, Willsky A. 1997. Tomographic reconstruction and estimation based on multiscale natural-pixel bases. *IEEE Trans. Image Process.* 6:463–78
111. Delaney A, Bresler Y. 1995. Multiresolution tomographic reconstruction using wavelets. *IEEE Trans. Image Process.* 4:799–813
112. Zhu WW, Wang Y, Deng YN, Yao YQ, Barbour RL. 1997. A wavelet-based multiresolution regularized least-squares reconstruction approach for optical tomography. *IEEE Trans. Med. Imaging* 16: 210–17
113. Deleted in proof
114. Sahiner B, Yagle A. 1987. Inversion of the Radon transform under wavelet constraints. In *Time-Frequency and Wavelets in Biomedical Signal Processing*, ed. M Akay, pp. 473–98. Piscataway, NJ: IEEE Press.
115. Olson T. 1992. Limited angle tomography via multiresolution analysis and oversampling. In *IEEE-SP Symp. Time-Frequency Time-Scale Anal*, pp. 215–18. Piscataway, NJ: IEEE Press
116. Donoho D. 1995. Nonlinear solution of linear inverse problems by wavelet-vaguelette decompositions. *J. Appl. Comput. Harmonic Anal.* 2(2):101–26
117. Bertero M. 1989. Linear inverse and ill-posed problems. In *Advances in Electronics and Electron Physics*. New York: Academic
118. Johnstone I, Silverman B. 1990. Speeds of estimation in positron emission tomography. *Ann. Stat.* 18:251–80
119. Johnstone I, Silverman B. 1991. Discretization effects in statistical inverse problems. *J. Complexity* 7:1–34
120. Kolaczyk E. 1996. A wavelet shrinkage approach to tomographic image reconstruction. *J. Am. Stat. Assoc.* 91:1079–90
121. Abramovich F, Silverman B. 1998. Wavelet decomposition approaches to statistical inverse problems. *Biometrika* 85(1): 115–29
122. Laine A, Schuler S, Fan J, Huda W. 1994. Mammographic feature enhancement by multiscale analysis. *IEEE Trans. Med. Imaging* 13:725–40.
123. Brake GM, Karssemeijer N. 1999. Single and multiscale detection of masses in digital mammograms. *IEEE Trans. Med. Imaging* 18:626–39
124. Giger ML. 1994. Computer-aided diagnosis. In *Med. Imaging V: Image Process. Proc. SPIE, San Jose, CA*
125. Daubechies I. 1990. The wavelet transform, time-frequency localization and signal analysis. *IEEE Trans. Inf. Theory* 36(5):961–1005
126. Laine A. 1991. Multiscale wavelet representations for mammographic feature analysis. In *Proc. Nat. Cancer Inst. Breast Imaging Workshop: State-of-the-Art New Technol., Image Enhance. Techn., Bethesda, MD*
127. Giger ML, Nishikawa RM, Doi K, Yi F, Vyborny CJ, et al. 1991. Development of

a smart workstation for use in mammography. In *Med. Imaging V: Image Process. Proc. SPIE, San Jose, CA*, pp. 101–3
128. Gordon R, Rangayyan RM. 1984. Feature enhancement of film mammograms using fixed and adaptive neighborhoods. *Appl. Opt.* 23:560–64
129. Morrow WM, Paranjape RB, Rangayyan RM. 1992. Region-based contrast enhancement of mammograms. *IEEE Trans. Med. Imaging* 11:392–406
130. Fan J, Laine A. 1996. Multiscale contrast enhancement and denoising in digital radiographs. See Ref. 4a, pp. 163–89
131. Barrett HH, Abley CK, Clarkson E. 1998. Objective assessment of image quality. III. ROC metrics, ideal observers, and likelihood-generating functions. *J. Opt. Soc. Am.* 15:1520–35
132. Martin JE, Moskowitz M, Milbrath JR. 1979. Breast cancer missed by mammography. *Am. J. Roentgenol.* 132:737–39
133. Bird RE, Wallace TW, Yankaskas BC. 1992. Analysis of cancers missed at screening mammography. *Radiology* 184: 613–17
134. Kegelmeyer WPK Jr, Pruneda JM. 1994. Computer-aided mammographic screening for spiculated lesions. *Radiology* 191: 331–37
135. Polakowski WE, Cournoyer DA, Rogers SK, Desimio MP, Ruck DW, et al. Computer-aided breast cancer detection and diagnosis of masses using difference of gaussians and derivative-based feature saliency. *IEEE Trans. Med. Imaging* 16: 811–19
136. Laine A, Song S. 1992. Multiscale wavelet representations for mammographic feature analysis. In *Math. Methods Med. Imaging, Proc. SPIE, San Diego, CA*, pp. 306–16
137. Laine A, Fan J, Schuler S. 1994. A framework for contrast enhancement by dyadic wavelet analysis. In *Digital Mammography*, ed. SMAAG Gale, DR Dance, AY Cairns, pp. 91–100. Amsterdam: Elsevier
138. Lu J, Healy DM Jr. 1994. Contrast enhancement of medical images using multiscale edge representation. In *Proc. SPIE: Wavelet Appl.*, pp. 711–19. Orlando, FL
139. Richardson JW. 1993. Wavelet packets applied to mammograms. In *SPIE, Biomed. Image Process. Biomed. Visualization, San Jose, CA*, pp. 504–8
140. Yoshida H, Zhang W, Cai W, Doi K, Nishikawa R, Giger ML. 1995. Optimizing wavelet transform based on supervised learning for detection of microcalcifications in digital mammograms. In *Proc. IEEE. Int. Conf. Image Process. Washington, DC*, pp. 152–55
141. Yoshida H, Nishikawa RM, Giger ML, Doi K. 1996. Signal/background separation by wavelet packets for detection of microcalcifications in mammograms. In *SPIE, Wavelet Appl. Signal Image Process. Denver, CO*, pp. 805–11
142. Laine A, Huda W, Chen D, Harris J. 1996. Segmentation of masses using continuous scale representations. In *Proc. Int. Workshop Mammogr. 3rd, Chicago, IL*, ed. R Schmidt, K Doi, ML Gigar, R Nishikawa, pp. 477–58. Amsterdam: Elsevier
143. Strickland RN, Hahn HI. 1995. Wavelet transform matched filters for the detection and classification of microcalcifications in mammography. In *Proc. Int. Conf. Image Process., Washington, DC.* pp. 422–25. Los Alanitos, CA: IEEE Comput. Soc.
144. Strickland RN, Hahn HI. 1996. Wavelet transforms for detecting microcalcifications in mammograms. *IEEE Trans. Med. Imaging* 15:218–29
145. Deleted in proof
146. Xing Y, Huda W, Laine A, Fan J. 1994. Simulated phantom images for optimizing wavelet-based image processing algorithms in mammography. In *Math Methods Med Imaging III, Proc. SPIE, San Diego. CA*, pp. 207–17
147. Xing Y, Huda W, Laine A, Fan J, Steinbach B. 1995. Comparison of a dyadic

wavelet image enhancement algorithm with unsharp masking and median filtering. In *Med. Imaging: Image Process. Proc. SPIE, San Diego, CA*, pp. 718–29

148. Chen D, Chang CM, Laine A. 1998. Detection and enhancement of small masses via precision multiscale analysis. In *Proc. Asian Conf. Comput. Vision, 3rd, Hong Kong*, pp. 192–99
149. Karssemeijer N, Brake GM. 1996. Detection of stellate distortions in mammograms. *IEEE Trans. Med. Imaging* 15: 611–19
150. Patrick N, Chang HP, Sahiner B, Wei D. 1996. An adaptive density-weighted contrast enhancement filter for mammographic breast mass detection. *IEEE Trans. Med. Imaging* 15:59–67
151. Patrick N, Chan HP, Wei D, Sahiner B, Helvie A, Adler DD. 1996. Automated detection of breast masses on mammograms using adaptive contrast enhancement and texture clasification. *Med. Phys.* 23:1685–96
152. Qian W, Li L, Clarke CL. 1999. Image feature extraction for mass detection in digital mammography: influence of wavelet analysis. *Med. Phys.* 26:402–8
153. Qian W, Li L, Clarke LP. 1999. Adaptive directional wavelet-based CAD method for mass detection. In *Computer-Aided Diagnosis in Medical Imaging*, ed. K Doi, H MacMahon, M L Giger, KR Hoffmann, pp. 253–57. Amsterdam: Elsevier.
154. Qian W, Li L, Clarke L, Clarke RA, JT. 1999. Digital mammography: comparison of adaptive and nonadaptive CAD methods for mass detection. *Acad. Radiol.* 6:471–80
155. Chen CH, Lee GG. 1997. Image segmentation using mutiresolution wavelet analysis and expectation-maximization (EM) algorithm for digital mammography. *Int. J. Imaging Syst. Technol.* 8:491–504
156. Zheng L, Chan AK, McCord G, Wu S, Liu JS. 1999. Detection of cancerous masses for screening mammography using discrete wavelet transform-based multiresolution Markov random field. *J. Digit. Imaging* 12:18–23
157. Heine JJ, Deans SR, Cullers DK, Stauduhar R, Clarke LP. 1997. Multiresolution statistical analysis of high-resolution digital mammograms. *IEEE Trans. Med. Imaging* 16:503–15
158. Miller L, Ramsey N. 1996. The detection of malignant masses by non-linear multiscale analysis. In *Digital Mammography'96*, ed. K Doi, ML Giger, RM Nishikawa, RA Schmidt, pp. 335–40. Amsterdam: Elsevier Sci.
159. Zwiggelaar R, Parr TC, Schumm JE, Hutt IW, Taylor CJ, et al. 1999. Model-based detection of spiculated lesions in mammograms. *Med. Image Anal.* 3:39–62
160. Kalman BL, Reinus WR, Kwasny SC, Laine A, Kotner L. 1997. Prescreening entire mammograms for masses with artificial neural networks: preliminary results. *Acad. Radiol.* 4:405–14
161. Broussard RP, Rogers SK, Oxley ME, Tarr GL. 1999. Physiologically motivated image fusion for object detection using a pulse coupled neural network. *IEEE Trans. Neural Netw.* 10:554–63
162. Dhawan A, Buelloni G, Gordon R. 1986. Enhancement of mammographic feature by optimal adaptive neighborhood image processing. *IEEE Trans. Med. Imaging* 5:8–15
163. Dhawan AP, Gordon R. 1987. Reply to comments on "enhancement of mammographic feature by optimal adaptive neighborhood image processing." *IEEE Trans. Med. Imaging* 6:82–83

Annual Review of Biomedical Engineering
Volume 2, 2000

CONTENTS